Materials Today Nano 33 (2026) 100726

Contents lists available at ScienceDirect

Materials Today Nano

journal homepage: www.sciencedirect.com/journal/materials-today-nano

Multifunctional dendrimer nanocarrier loaded with ibuprofen for synergistic personalized theranostics and targeted ablation in breast cancer

Shadab Dabagh [a], Hamed Ghorbanpoor [b,c], Merve Nur Soykan [b,d], Ayla Eker Sarıboyacı [b,c], Barbara Adinolfi [a], Ambra Giannetti [a], Zesen Li [e], Ni Lan [e], Bai-Ou Guan [e], Hüseyin Avci [b,f,g,*], Yang Ran [e,**], Francesco Chiavaioli [a,***]

[a] Institute of Applied Physics "Nello Carrara", National Research Council of Italy (CNR), Sesto Fiorentino, FI, 50019, Italy
[b] Cellular Therapy and Stem Cell Production Application and Research Centre, ESTEM, Eskisehir Osmangazi University, Eskisehir, 26480, Türkiye
[c] Department of Biomedical Engineering, Faculty of Engineering and Architecture, Eskisehir Osmangazi University, Eskisehir, 26040, Türkiye
[d] Department of Stem Cell, Institute of Health Sciences, Eskisehir Osmangazi University, Eskisehir, 26040, Türkiye
[e] Guangdong Provincial Key Laboratory of Optical Fiber Sensing and Communications, Institute of Photonics Technology, Jinan University, Guangzhou, 510632, China
[f] Department of Metallurgical and Materials Engineering, Eskisehir Osmangazi University, Eskisehir, 26040, Türkiye
[g] Translational Medicine Research and Clinical Center (TATUM), Eskişehir Osmangazi University, Eskisehir, 26040, Türkiye

ARTICLE INFO

Keywords:
Breast cancer
Multifunctional dendrimer nanocarrier
Theranostics
Hyperthermia
MRI contrast agent
Ibuprofen

ABSTRACT

Cancer remains a leading global health challenge, causing nearly 10 million deaths annually. We report a multifunctional magnetite-based dendrimer nanocarrier ($MAGSiAG_1$) and its ibuprofen-loaded form (IBU@-$MAGSiAG_1$) for synergistic anti-cancer, anti-inflammatory, hyperthermia, and diagnostic applications. FTIR, XRD, TGA, DLS, and zeta potential analyses confirm successful sequential functionalization, dendrimer formation, and ibuprofen loading, resulting in spherical nanocarriers with an average hydrodynamic size of 70 nm and near-neutral surface charge (−39 mV) suitable for tumor penetration and systemic stability. VSM measurements reveal superparamagnetic behavior with saturation magnetization decreasing from 75 emu/g to 35–40 emu/g, ensuring strong magnetic responsiveness while maintaining colloidal stability. Under an alternating magnetic field (150 Oe), IBU@MAGSiAG1 achieves therapeutic temperatures (~45 °C) via *Néel* and *Brownian* relaxation. *In vitro* relaxivity measurements showcase high T2 relaxivity coefficient ($r_2 = 358.88 \pm 5$ mM^{-1} s^{-1} for MAG-SiAG1, 335 ± 49.8 mM^{-1} s^{-1} for IBU@MAGSiAG1), empowering effective MRI contrast. Drug loading efficiency exceeds 90%, with pH-responsive release profile that demonstrates accelerated ibuprofen release in acidic conditions (tumor-mimicking pH 5.0–6.5) and slower release at physiological pH (~7.4). Cytotoxicity studies on MCF-7 human cancer cells reveal good viability (85–90%) at 250–400 μg/mL of drug concentration range, while higher concentrations (~400 μg/mL) reduce viability to ~60%, indicating therapeutic potential. Good biocompatibility of the developed nanocarriers is attained using with EA.hy926 endothelial cells, ensuring safe systemic delivery. Overall, IBU@MAGSiAG1 showcases high multifunctionality by integrating hyperthermia, controlled drug release, and MRI contrast into a single platform, paving the way for novel therapeutic targeted treatments in cancers that might advance personalized medicine approaches.

1. Introduction

Magnetite nanocarriers (Fe_3O_4NPs) have garnered significant attention in biomedicine due to their versatility in a broad range of applications [1]. These nanocarriers leverage the ability to selectively bind to biological targets, and hence are extremely useful for diagnostics and treatments [2–6]. In addition, they feature biocompatibility and minimal cytotoxicity to human cells, thus making them suitable for integration in clinical settings [7]. By applying an external magnetic field, these nanocarriers can precisely be directed to the target, thus offering a controlled approach to therapeutic and diagnostic purposes, such as hyperthermia [8–10] and targeted drug delivery [11–14],

* Corresponding author.
** Corresponding author.
*** Corresponding author.
E-mail addresses: havci@ogu.edu.tr (H. Avci), tranyang@jnu.edu.cn (Y. Ran), f.chiavaioli@ifac.cnr.it (F. Chiavaioli).

https://doi.org/10.1016/j.mtnano.2025.100726
Received 26 September 2025; Received in revised form 14 November 2025; Accepted 1 December 2025
Available online 2 December 2025
2588-8420/© 2025 The Authors. Published by Elsevier Ltd. This is an open access article under the CC BY license (http://creativecommons.org/licenses/by/4.0/).

particularly in cancer therapy and diagnostics combined with magnetic resonance imaging [15–18] and biosensors [19–24]. These magnetic contrast agents are crucial in MRI, which dramatically enhance the contrast between regions of interest and healthy tissues [25]. Magnetite nanocarriers as a contrast agents can increase the level of signals in T2-weighted MRI and can also reduce T1 relaxation times. These features leverage the functionality and biocompatibility of these nanocarriers given their polymeric shell, which provides reactive functional groups for conjugation with biomolecules transferring them to target tissues and reducing adverse effects on healthy cells [26,27]. On the other hand, hyperthermia is a controlled treatment that raises tissue temperatures from 41 °C to 45 °C in order to increase the susceptibility of cancer cells to temperatures [28]. This approach can be used alone or in combination with other therapies, resulting in positive outcomes for poorly controlled and metastasized cancers, and aiding in post-surgery rehabilitation [29]. MRI can accurately calibrate temperature changes, making hyperthermia more effective and reliable when guided by MRI [30]. However, magnetic hyperthermia and MRI agents are still in the implementing phase, facing challenges such as stability, biocompatibility, clearance mechanisms, effective targeting, tumor heterogeneity, and variability in patient responses [31]. To minimize side effects, it is essential to employ an optimal dose calculation strategy [32]. One promising approach to address these challenges is the functionalization and polymerization of magnetite nanocarriers, which can help in the control over these issues [33]. The functionalization with silica-based nanoparticles has shown promise behavior in biomedical applications, improving biocompatibility, stability, and targeted delivery capabilities [34]. Noncovalent surface functionalization reduces complement activation and macrophage uptake, while biopolymers like fucoidan promote osteogenic differentiation. Coated nanocarriers have potential in drug delivery, cancer therapy, magneto hyperthermia, bioimaging, and diagnostic applications [35,36]. (3-Aminopropyl)triethoxysilane (APTES) is a versatile agent used in nanoparticle functionalization, offering efficient surface modification, enhanced biocompatibility, and improved stability. Its high drug-loading capacities and controlled release kinetics make it ideal for advanced drug delivery systems and MRI, making it a valuable tool for biomedical applications [37–39]. Cyanuric chloride (CC) and diethylenetriamine (DETA) functionalization approaches have been used in various applications, including enzyme immobilization, drug delivery, and composite material enhancement. CC has enabled covalent immobilization of enzymes like tyrosinase and pectinase, resulting in robust nano biocatalysts with improved stability and performance [40,41]. Triazine-based dendrons, including DETA, have been applied to magnetic nanoparticles to achieve high adsorption capability, demonstrating potential for drug delivery [40,42–44]. Between different type of polymers, dendrimers are innovative polymeric structures that enable precise functionalization of magnetite nanocarriers, making them perfectly suitable for advanced therapeutic applications, such as gene delivery and cancer treatment [45]. Their highly branched, monodisperse, and precisely controllable structure provides high density of functional groups, enabling the encapsulation or conjugation of multiple drug molecules, and hence enhancing drug loading capacity compared to linear polymers [46]. The hydrophobic inner part of dendrimers empowers the solubility and bioavailability of poorly soluble drugs, while surface functionalization with targeting ligands allows specific binding of receptors on cancer cells, enabling targeted delivery [47]. Dendritic polymers are created around the core and marked with [G-n], where n indicates the generation number in the structure on the right side. Dendrimers, with $G < 4$ and $G \geq 4$, are low and high generation dendrimers, with the dendrimer core sometimes referred to as zero generation [48]. Dendrimer would leverage the degree of loading the drug on the surface of the carrier that is critical for medical applications. Poly(amidoamine) (PAMAM) dendrimers are promising given their unique structural properties that enable the creation of multifunctional nanocarriers and sensors. They have been used to functionalize nanocarriers like hydroxyapatite for bone tissue engineering, silica nanocarriers for photoluminescence sensing, and carbon dots for cancer diagnosis and therapy, with subsequent surface modifications to empower stability, reduce toxicity, and improve therapeutic efficiency [49–52].

Among drugs, ibuprofen (IBU) that is classified as a nonsteroidal anti-inflammatory drug (NSAID) and is routinely used to alleviate pain caused by headaches, kidney stones, osteoarthritis, postoperative pain, and arthritis [53], offers several advantages over other anti-inflammatory and chemotherapeutic agents due to its excellent pharmacokinetic profile, safety, and therapeutic versatility. Recent findings have shown that consuming 200 mg of IBU on a daily basis might lower the chance of developing cancer [54,55]. Moreover, compared to NSAIDs like acetylsalicylic acid and ketorolac, IBU shows lower risks of thrombosis and hepatotoxicity, making it safer for long-term use [56,57], and has stronger anticancer properties, particularly in relation to breast cancer [58]. Furthermore, research on pH-responsive nanocarriers based on IBU highlights their efficacy in inhibiting primary tumor growth and metastasis, combining the benefits of nonsteroidal anti-inflammatory medicine and chemotherapy for enhanced therapeutic outcomes in experimental tumor models [59]. Similarly, redox-sensitive hyaluronic acid-IBU mixtures have been developed for delivering doxorubicin, showcasing advantages such as on-demand drug release, favorable biodistribution, and improved therapeutic efficacy against metastatic breast cancer [60]. Further advancements include an IBU-conjugated amphiphilic deblock copolymer forming nano micelles for co-delivering doxorubicin, which enables sustained drug release and increased antitumor activity compared to free doxorubicin [61]. Another approach involves tethering IBU to a hydrogel matrix via esterification, which provides controlled, localized drug release, while retaining its biological activity, and hence expanding its range of clinical applications [62]. Collectively, these attributes make IBU an ideal model drug for evaluating multifunctional nanocarrier-based systems in anti-inflammatory and anticancer therapies, combined with hyperthermia applications [54,63,64].

A therapeutic improvement due to IBU release from a magnetite-based dendrimer nanocarrier under an alternating magnetic field arises from the synergistic effect between magnetothermal activation and pH-responsive drug release [65]. Under alternating magnetic field, the magnetic core of the nanocarrier generates localized heat through *Néel* and *Brownian* relaxation losses, elevating the temperature of the surrounding medium. Localized hyperthermic effect (about 41–45 °C) enhances the permeability of cell membranes for nanocarrier uptake and weakens interactions between drug and the dendrimer surface, promoting drug desorption [66–68]. Dendrimers are rich in amine and amide groups and cause to thermal-responsive reservoirs that accelerate IBU release under acidic environments (typical of tumor tissues) [69]. This process, coupled with hyperthermia, enhances apoptotic signaling in tumor cells by inducing thermal stress, while reducing systemic toxicity [70]. This dual synergistic mechanism of magnetically controlled heating and targeted drug release improves therapeutic efficacy against cancer cells in comparison to other approaches. Therefore, the development of multifunctional nanocarriers is crucial for advancing cancer treatment by enabling targeted drug delivery, effective imaging, and therapeutic interventions such as hyperthermia. The literature accounts for different types of magnetite-based nanocarriers based on mesoporous Fe_3O_4 nano/microspheres [71], xanthan gum/Fe_3O_4 hydrogels [72], and Fe_3O_4@SiO_2 core/shell nanoparticles [73]. While these approaches showcased moderate MRI contrast and effective drug loading, they lacked the combination of high relaxivity, rapid hyperthermia, and pH-controlled and alternating magnetic field-responsive drug release.

Here, magnetite (Fe_3O_4) (MAG) nanocarriers were functionalized with SiO_2, APTES, and dendrimer generation 1 (G1) ($MAGSiAG_1$ dendrimer nanocarrier) and then were successfully synthesized through a chemical method due to its precision in controlling particle size, surface modification, and functional group integration. All these features are

critical for achieving the desired properties for targeted drug delivery, imaging, and hyperthermia applications. Therefore, the proposed MAGSiAG1-based nanocarrier clearly demonstrates superior multifunctionality with respect to the state-of-the-art. Moreover, IBU was subsequently loaded onto this nanocarrier to explore their therapeutic potential against breast cancer, alongside their dual functionality in MRI and hyperthermia applications. The drug release behavior was investigated by varying the pH to elucidate the influence of dendrimer functionalization on release kinetics. The cell viability and cytotoxicity of the dendrimer nanocarrier were evaluated using the 3-[4,5-dimethylthiazol-2-yl]-2,5-diphenyl tetrazolium bromide (MTT) test before and after IBU loading on human breast cancer cells (MCF-7) and endothelial cells (EA.hy926). As the main objective is targeted ablation in breast cancer, the assessment of cytotoxicity on EA.hy926 was crucial, since the nanocarriers definitely interacted with vascular endothelial cells before reaching the tumor. This enabled to identify a safe and optimal concentration range for *in vitro* MRI and hyperthermia applications at nanocarrier concentrations below the toxic threshold.

2. Experimental section

2.1. Chemicals

The materials used include high-purity starter material, functionalization agents, and solvents that were employed during various steps. All chemicals were of ≥99% purity with the details provided in Supplementary Material (SM1).

2.2. Preparation of dendrimer nanocarrier and ibuprofen loading

Fe_3O_4 nanoparticles were synthesized by dissolving $FeCl_3{\cdot}6H_2O$, followed by a series of steps to coat with silica, functionalize with APTES and cyanuric chloride, and finally graft dendrimers using DETA and PAMAM. IBU was then loaded onto the final nanocarrier using sonication and stirring. Drug release studies were conducted under different pH conditions, and release percentages were calculated. These processes are thoroughly detailed in Supplementary Material (SM2).

2.3. Characterization of the multifunctional dendrimer nanocarrier

The synthesized $MAGSiAG_1$ dendrimer nanocarriers were characterized using various spectroscopy and microscopy techniques. Details of the instruments are provided in Supplementary Material (SM3).

2.4. Biological and morphological assessment of the multifunctional dendrimer nanocarrier

MCF-7 and EA. hy926 cells were treated with $MAGSiAG_1$ and $IBU@MAGSiAG_1$ nanocarriers, cell viability was assessed via MTT assay, and fluorescence microscopy was employed to visualize the changes between viable cells. These *in vitro* assays are essential because they allow for rapid, high-throughput, and cost-effective initial screening of nanoparticle characteristics, toxicity, and drug release, providing the foundation for further studies in animal models [74]. MRI phantom studies demonstrated the T2-weighted contrast at varying concentrations, with relaxivity coefficient (r_2) analyzed using T2-weighted imaging. Hyperthermia efficiency of $IBU@MAGSiAG_1$ was tested under an alternating current (AC) magnetic field, and the specific absorption rate (SAR) was calculated. Post-hyperthermia, cell viability for MCF7 and EA.hy926 endothelial cells were assessed to evaluate therapeutic potential. Detailed explanation and developed protocols of assessment are provided in Supplementary Material (SM4 and SM5).

Fig. 1 sketches the preparation of $IBU@MAGSiAG_1$ dendrimer nanocarrier involving the synthesis of dendrimer component and the loading of IBU, followed by its characterization and MTT-assisted cytotoxicity test for potential use in cancer diagnosis (MRI imaging)

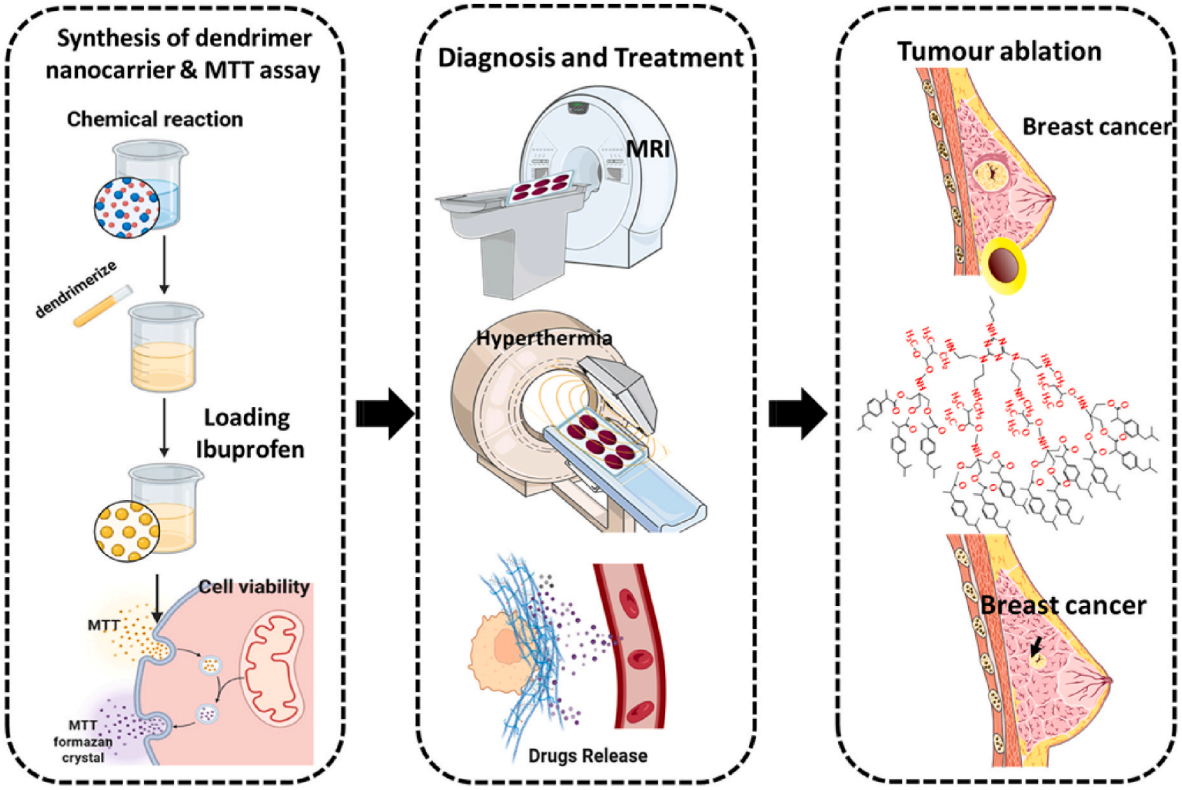


Fig. 1. Preparation, characterization and assessment of the $IBU@MAGSiAG_1$ dendrimer nanocarriers. The whole process starts from the synthesis from raw materials, then cytotoxicity assessment using the MTT test, up to diagnostic and treatment applications as MRI-improved contrast agent, hyperthermia, drug release and tumor ablation.

and related treatment (hyperthermia, drug delivery and tumor ablation). The developed multifunctional nanocarriers showed remarkable results in terms of drug release, imaging capabilities, and hyperthermia performance, paving the way to personalized medicine and targeted treatments in the worldwide challenge against cancer.

3. Results and discussion

3.1. Spectral and elemental characteristics of the multifunctional dendrimer nanocarrier

The FTIR spectra are shown in Fig. 2a where the critical insights into the sequential synthesis, surface functionalization, and loading of IBU onto Fe_3O_4@SiO_2-APTES-CC-$G_{0.5}$/G_1 dendrimer nanocarriers were successfully attained. The spectrum corresponding to magnetite nanoparticles exhibits a characteristic peak at ~580 cm^{-1}, confirming the Fe-O stretching vibration typical of the magnetic core [75]. Upon silica

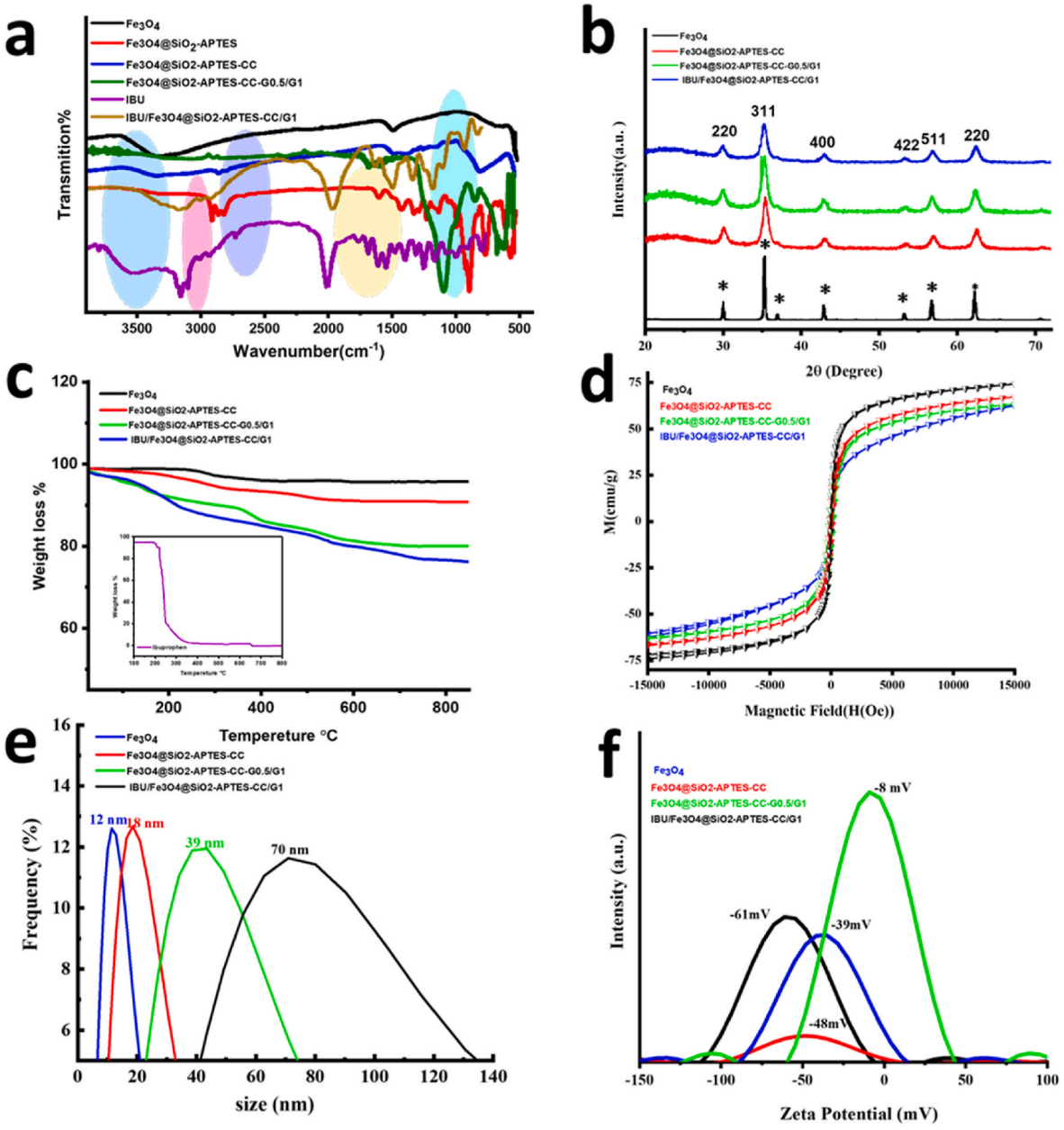


Fig. 2. Comprehensive characterization of IBU@MAGSiAG$_1$ dendrimer nanocarriers at different synthesis stages. **(a)** FTIR spectra with the successful functionalization of nanocarrier. The highlighted regions demonstrate specific interactions and molecular vibrations introduced during functionalization. **(b)** XRD patterns showing the crystalline nature of magnetite with characteristic peaks positions across samples and confirming the magnetic core's crystal structure retained after surface modifications. **(c)** TGA analysis for the evaluation of the thermal stability and composition of organic coatings (e.g., APTES, IBU) in functionalized samples compared to the bare. **(d)** VSM magnetization curves showing the superparamagnetic behavior of dendrimer nanocarriers and a decrease in saturation magnetization with surface modifications due to non-magnetic coatings, while hysteresis-free loops confirm the materials' suitability. **(e)** DLS analysis displaying particle size distributions. **(f)** Zeta potential measurements accounting for the surface charge of particles and confirming the surface chemistry changes due to functionalization, and subsequent IBU encapsulation.

coating (Fe_3O_4@SiO_2-APTES), new peaks at ~1080 cm^{-1}, which can be attributed to Si-O-Si stretching vibrations, and a broad peak at ~3300–3400 cm^{-1} that corresponds to O-H stretching from hydroxyl groups on the silica surface appear [76]. The peaks at ~2920–2850 cm^{-1} confirm the presence of C-H stretching vibrations from the APTES organic groups, indicating successful silanization [77]. Functionalization with CC (Fe_3O_4@SiO_2-APTES-CC) introduces a peak at ~1700 cm^{-1}, which can be attributed to C=O stretching vibrations of carbonyl groups, along with broadening in the ~3300–3400 cm^{-1} region due to hydroxyl groups [78]. The subsequent dendrimer formation (Fe_3O_4@-SiO_2-APTES-CC-$G_{0.5}/G_1$) is confirmed by the appearance of peaks at ~1650 cm^{-1} and ~1550 cm^{-1}, which correspond to Amide I (C=O stretching) and Amide II (N-H bending) vibrations, respectively [79]. These peaks validate the successful formation of amide bonds, a key feature of dendrimer functionalization. Pure IBU displays its characteristic peaks, including a sharp peak at ~1720 cm^{-1} (C=O stretching) from the carboxylic acid group and a broad peak at ~2950 cm^{-1} (O-H stretching), which is indicative of its hydroxyl group [80]. After IBU loading onto the nanocarrier (IBU/Fe_3O_4@SiO_2-APTES -CC-G_1), the retention of the IBU-specific peak at ~1720 cm^{-1} confirms the presence of the drug on the nanocarrier. The broadening of the ~3300–3400 cm^{-1} peak suggests hydrogen bonding interactions between IBU molecules and the functional groups on the nanocarrier surface [81]. Notably, a reduction in the intensity of the amide peaks (~1650 cm^{-1} and ~1550 cm^{-1}) indicates partial coverage of the dendrimer amide groups by IBU molecules, further supporting successful drug loading. The structural characteristic, surface functionalization, and IBU loading onto Fe_3O_4@SiO_2-APTES-CC-$G_{0.5}/G_1$ dendrimer nanocarriers are also illustrated in Fig. 2b by XRD pattern. The bare magnetite nanoparticles show the characteristic peaks at 2θ values of ~30.1°, ~35.5°, ~43.1°, ~53.4°, ~57.0°, and ~62.6°, which refer to the (220), (311), (400), (422), (511), and (440) crystal planes, respectively. These peaks match the spinel cubic structure of Fe_3O_4 (JCPDS No. 19–0629), confirming the crystalline nature of the magnetic core [82]. After surface modification with silica and subsequent functionalization, the XRD patterns retain the prominent Fe_3O_4 diffraction peaks, indicating the structural integrity of the core. However, a slight reduction in peak intensity is observed, which can be attributed to the amorphous silica layer and organic moieties (e.g., APTES and dendrimers) on the nanoparticle surface. This reduction confirms successful coating and functionalization without compromising the magnetic core's crystalline structure. IBU-loaded Fe3O4@SiO_2-APTES-CC-G_1 shows similar diffraction peaks associated with Fe_3O_4, confirming that the crystalline core remains intact after drug loading. The absence of additional peaks in the IBU-loaded sample spectrum suggests that the IBU is in an amorphous or molecularly dispersed form rather than crystalline, which feature benefits from drug delivery applications, as it enhances drug solubility and bioavailability [83]. The thermogravimetric analysis (TGA) graph in Fig. 2c reveals the weight loss behavior of various functionalized magnetite and IBU-loaded nanoparticles. The magnetite nanoparticles exhibit low weight loss (<5%) throughout the temperature range, indicating high thermal stability with only surface-adsorbed water being removed [71]. In contrast, the ones functionalized with SiO_2, APTES, and CC show distinct stages of weight loss: ~3–5% between 100 and 200 °C (moisture and volatile removal), ~5–10% from 200 to 500 °C (decomposition of APTES and CC), and ~1–3% gradual loss from 500 to 800 °C due to residual organic breakdown [84]. Further functionalization with $G_{0.5}/G_1$ dendrimers leads to greater weight loss, with ~3–5% loss in the 100–200 °C range (moisture removal), ~10–20% between 200 and 500 °C (dendrimer decomposition), and ~3–5% in the 500–800 °C range, underscoring core thermal stability [85]. The IBU-loaded Fe_3O_4@SiO_2-APTES-CC/G_1 samples exhibit significant weight loss due to IBU degradation, with ~5% loss in the 100–200 °C range (moisture and loosely bound IBU), ~20–30% between 200 and 300 °C (major IBU decomposition), ~10–15% between 300 and 500 °C (further breakdown of functional groups), and ~5–8% from 500 to 800 °C (core stability). The inset showing pure IBU highlights its primary decomposition between 200 and 300 °C, with ~70–80% weight loss, and negligible changes thereafter, indicating residual ash [86]. The comparative analysis reveals that functionalization and IBU loading significantly influence thermal stability, with the dendrimer and IBU contributing to distinct degradation patterns. For ensuring that the nanoparticles do not retain magnetization in the absence of an external magnetic field, which is vital for avoiding aggregation in biological environments, the vibration samples were characterized with magnetometer and the results are shown in Fig. 2d. The magnetite nanoparticles exhibit the highest saturation magnetization (M_s) of approximately 75 emu/g, ensuring strong magnetic properties, and the coercivity (H_c) is close to 0 Oe, confirming superparamagnetic behavior. The high M_s of magnetite makes it ideal for applications requiring strong magnetic responses, such as magnetic hyperthermia and MRI [87]. After silica coating and functionalization with APTES, the M_s decreases to around 50–55 emu/g. This reduction in M_s stems from the fact that the silica layer and organic functional groups are non-magnetic, effectively diluting the magnetic core contribution to the overall magnetization [83]. However, the H_c remains low, preserving the superparamagnetic characteristics. The silica coating offers a biocompatible surface and inhibits particle aggregation, while the APTES functionalization incorporates amine groups, enabling further chemical conjugation for drug release or targeting [87,88]. In the Fe_3O_4@SiO_2-APTES-CC-$G_{0.5}/G_1$ system, the saturation magnetization further decreases to approximately 40–45 emu/g. The addition of dendrimer layers (generations $G_{0.5}/G_1$) introduces additional non-magnetic organic material, which increases the overall particle size but reduces the proportion of the magnetic core relative to the total particle volume. Despite this reduction, the superparamagnetic behavior (low H_c) is preserved, which is critical for ensuring controlled magnetization during external field application. The dendrimers provide functional groups that enhance drug-loading capacity and biocompatibility, making the nanoparticles more versatile for biomedical applications [89]. In the case of IBU/Fe_3O_4@-SiO_2-APTES-CC/G_1, the M_s decreases further to approximately 35–40 emu/g. This reduction reflects the successful loading of IBU, a non-magnetic drug, onto the functionalized nanoparticles. The functional groups introduced by dendrimers facilitate efficient drug binding, while the silica coating ensures stability and compatibility in physiological environments. H_c remains negligible, which is advantageous for applications requiring transient magnetic responses, such as in MRI and hyperthermia. The decrease in M_s with each functionalization step can be explained by the addition of non-magnetic materials (silica, APTES, dendrimers, and IBU), which increase the total particle volume but reduce the proportion of the magnetic core. The dynamic light scattering (DLS) graph is reported in Fig. 2e, where the particle size distribution for Fe_3O_4 nanoparticles and their progressively functionalized forms are detailed. The magnetite nanoparticles exhibit the smallest size distribution with an average diameter of 12 nm after fine dispersion, reflecting their intrinsic nanoscale size and uniformity. The introduction of SiO_2 and APTES functional layers increases the average particle size to 18 nm, which can be attributed to the formation of a silica shell and the subsequent binding of APTES molecules [83]. Following the dendrimer coating, the particle size increases significantly to 39 nm, reflecting the deposition of $G_{0.5}/G_1$ dendrimer layers. This step not only enlarges the nanoparticles, but also provides abundant functional groups for drug loading and conjugation with bioactive molecules [87]. In the last step, IBU loading onto Fe_3O_4@SiO_2-APTES-CC/G_1 results in a marked increase in the particle size to 70 nm, as also observed previously [90]. Despite this increase, the nanocarriers remain within the optimal nanoscale range (<100 nm) for tumor penetration via the enhanced permeability and retention (EPR) effect [91]. Therefore, the size remains suitable for efficient accumulation at tumor sites, while the slightly larger hydrodynamic diameter facilitates higher drug loading, improved stability during circulation, and controlled release at the tumor microenvironment. Furthermore, the dendrimer functionalization provides

abundant surface functional groups that enhance cellular uptake through endocytosis, improving intracellular delivery of IBU and thereby maximizing therapeutic efficacy at the tumor site [92]. This substantial size increases due to the IBU loading benefits from drug delivery, while maintains a size range suitable for hyperthermia and MRI applications, highlighting their potential for multifunctional theranostic applications. The zeta potential in Fig. 2f details the surface charge of the samples at different stages of the functionalization process, from stability, MRI, and up to hyperthermia applications. The bare magnetite nanoparticles show a zeta potential of approximately −61 mV, indicating a highly negative surface charge. This significant charge is primarily due to hydroxyl groups on the nanoparticle surface, contributing to colloidal stability through strong electrostatic repulsion [93]. After silica coating and functionalization with APTES, the zeta potential becomes less negative, decreasing to approximately −48 mV. The silica coating introduces silanol groups, which slightly neutralize the surface charge, while the presence of APTES adds amine groups that might further reduce the net negative charge [94]. Although the zeta

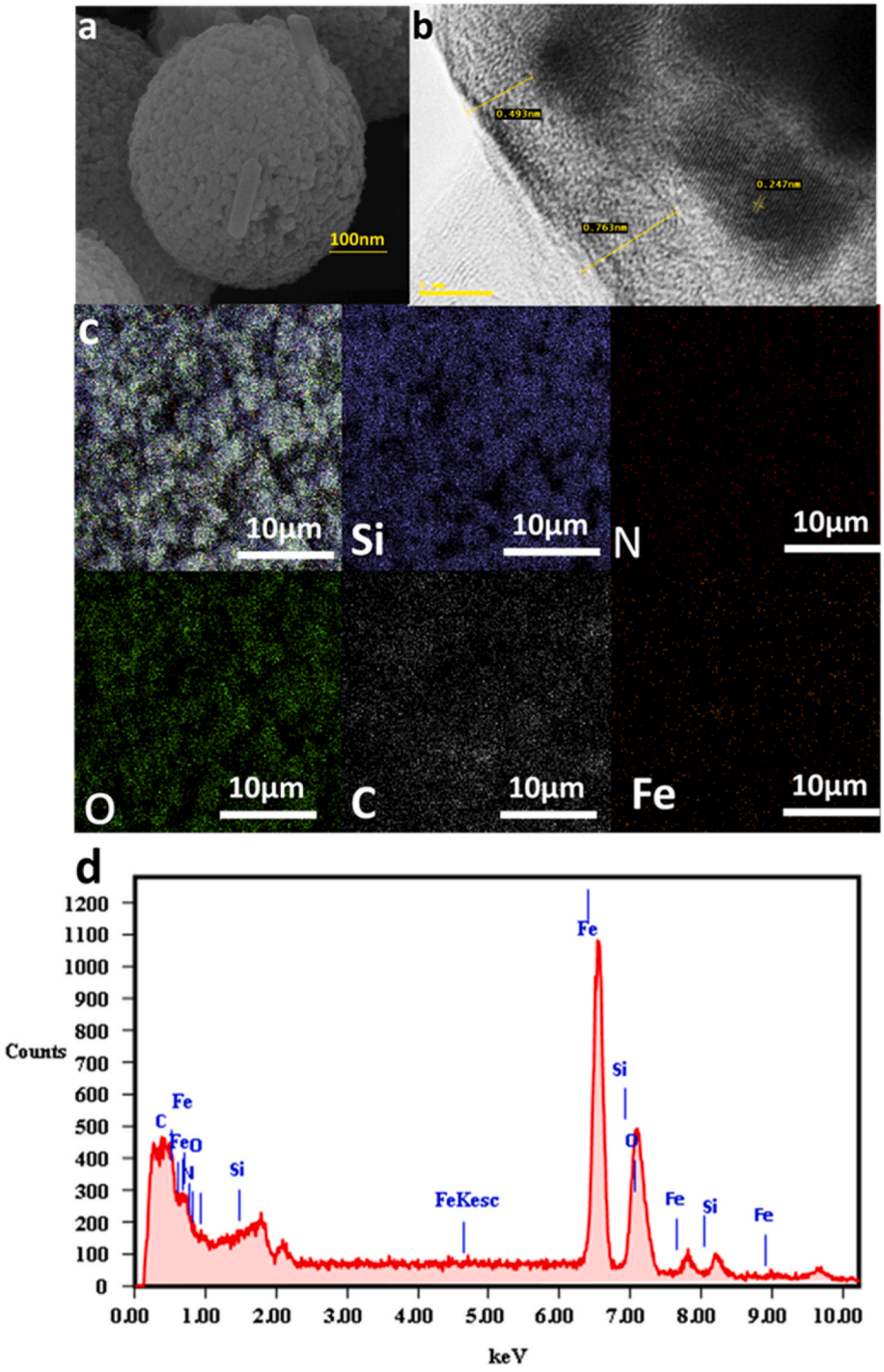


Fig. 3. Characterization of the synthesized IBU@MAGSiAG$_1$ dendrimer nanocarrier. **(a)** SEM image showing the spherical morphology of the nanocarrier with rough surface texture (scale bar: 100 nm). **(b)** HRTEM image displaying the lattice fringes with measured interplanar spacings of 0.493 nm, 0.763 nm, and 0.247 nm, which indicate the crystalline structure. **(c)** Elemental mapping images confirming the uniform distribution of elements Si, N, O, C, and Fe across the nanocarrier. **(d)** EDX spectrum verifying the elemental composition of the nanocarrier, with prominent peaks corresponding to Fe, Si, O, and minor peaks for C, N.

potential decreases, the nanoparticles remain sufficiently stable due to the moderate surface charge, which prevents aggregation. The silica coating also enhances biocompatibility and provides a platform for further functionalization. The addition of dendrimers ($G_{0.5}/G_1$ generations) results in a dramatic shift in the zeta potential to approximately −8 mV, indicating a near-neutral surface charge [95]. Dendrimers contain multiple functional groups that can partially shield the surface charge, leading to this significant reduction [96]. For hyperthermia, the functionalization with dendrimers allows for enhanced targeting and drug delivery capabilities, although additional stabilizing agents might be necessary to prevent aggregation during treatment. Upon loading IBU onto the dendrimer-functionalized nanoparticles, the zeta potential increases again to approximately −39 mV, indicating a partial restoration of the negative charge. This increase improves colloidal stability compared to the dendrimer-coated nanoparticles, ensuring better dispersion in biological fluids.

Fig. 3a displays a FESEM image of Fe_3O_4@SiO_2-APTES-CC-$G_{0.5}/G_1$ nanoparticles. The particles exhibit a spherical morphology with a uniform size distribution [79,97,98], with an average particle size of roughly 50 nm that is consistent with expectations for nanoparticles designed for biomedical applications [99]. The surface appears rough, indicative of the silica coating and dendrimer functionalization. Fig. 3b shows a TEM image of the final product after IBU loading. High-resolution analysis reveals clear lattice fringes with interplanar spacings of 0.493 nm, 0.763 nm, and 0.247 nm, corresponding to the crystalline planes of magnetite [100]. The TEM image confirms the spherical morphology of nanoparticles post-IBU loading, indicating that the drug loading process does not alter the morphology or core-shell structure. Fig. 3c provides elemental mapping of the nanocarriers in the presence of silica shell coating and of amine groups from APTES and dendrimers. The next subfigure refers to oxygen in both magnetite and silica, while carbon that comes from organic groups (dendrimers and loaded IBU) is detailed in the next subfigure [101]. Fe mapping clearly localizes it in the core, representing the Fe_3O_4 magnetic nanoparticles. The uniform distribution of Si, N, and Fe confirms the successful synthesis of core-shell nanoparticles and relative functionalization with APTES and dendrimers. The EDX spectrum in Fig. 3d confirms the elemental composition of the nanoparticles. Peaks corresponding to Fe, Si, O, and N are clearly visible, validating the presence of Fe_3O_4 as the core, a silica shell, and APTES/dendrimer functionalization [102]. It should be underscored that the absence of any unexpected element indicates the high purity of the materials produced. The presence of carbon and nitrogen further successfully confirms dendrimer formation and IBU loading. These results remarkably demonstrate the effectiveness and reliability in synthesis and characterization, with its spherical morphology aids in empowering drug-loading capacity.

3.2. Drug dosage analysis

Fig. 4 reports the outcomes related to the synthesized IBU@-$MAGSiAG_1$ dendrimer nanocarriers in terms of calibration curve analysis and drug loading studies, which are performed to quantify the encapsulated drug content and to evaluate the nanocarrier efficiency for controlled drug delivery applications. Fig. 4a depicts the calibration curve with a linear trend showing the relationship between the absorbance at 266 nm and the concentration of IBU in (mg/L). The very high correlation coefficient ($R^2 = 0.99$) indicates a strong linear correlation, validating the method for quantifying IBU in solution. This curve is used to calculate the IBU concentration during both loading and release studies, ensuring accurate measurements of the drug behavior [103,104]. During the loading process, when the loading measurements are taken using the above protocol, the percentage of loading is consistently above 90% at pH 7 that is in agreement with other works [105,106]. The drug release in delivery systems is significantly influenced by pH levels, impacting therapeutic efficacy under varying physiological conditions. pH levels below 6.8, which are characteristic of the acidic tumor microenvironment, facilitate rapid release of therapeutic agents, whereas minimal release occurs at physiological pH levels around 7.4 [107–109]. This pH-dependent behavior is particularly beneficial in targeting cancer therapies, as tumors often exhibit an acidic extracellular environment [110,111]. In contrast, in more neutral to alkaline conditions (approximately pH 7–8.5), enhanced drug release is due to increased solubility of the drug, allowing for effective release after passing the gastric phase [112,113]. The intricate relationship between pH levels and drug release mechanisms is vital for optimizing therapeutic outcomes in various medical applications. Fig. 4b shows the release profiles of IBU from the $MAGSiAG_1$ nanocarriers that are studied in buffer solutions of varying pH (1.2, 5.4, 7.2, and 8.5) over 24 h. In the pH 1.2 (acidic), the drug reports the highest release (~60% within 8 h), stabilizing thereafter [114,115]. This behavior can stem from the increased solubility of IBU in an acidic environment, which enhances desorption from the nanoparticle surface. At pH 5.0 (mildly acidic), a moderate release (~40% at 24 h) is observed, showing slower kinetics compared to pH 1.2. This reflects reduced IBU solubility and weaker interactions between the drug and the carrier in this pH. At pH 7.4 (neutral), the release is further reduced (~30% at 24 h). In fact, in physiological pH conditions, IBU exhibits slower release kinetics due to the relatively stable interactions with the nanocarriers. At pH 8.5 (basic), the lowest release (~15% at 24 h) is observed. The basic environment reduces drug solubility and slows down the desorption of IBU from the carrier surface [116]. The $MAGSiAG_1$ functional groups create hydrophobic and electrostatic interactions that facilitate IBU adsorption. IBU loading occurs through hydrophobic and electrostatic

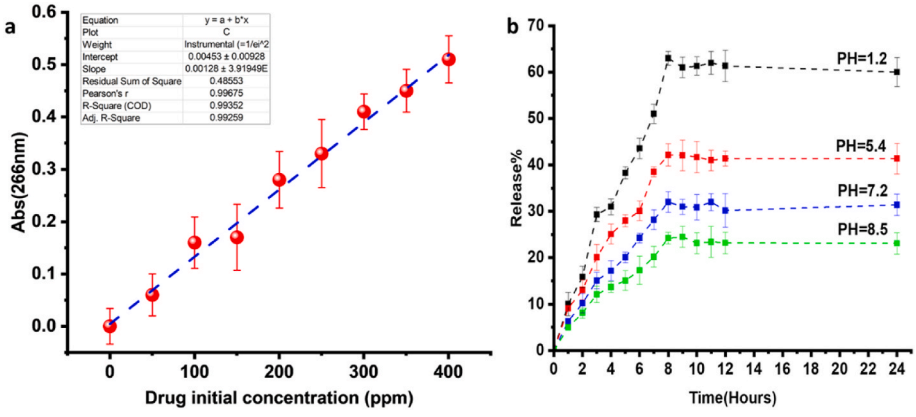


Fig. 4. (a) Calibration curve for drug quantification at 266 nm, showing a linear relationship between drug concentration (ppm) and absorbance with high correlation ($R^2 = 0.99$). **(b)** Drug release profiles over 24 h at varying pH conditions (pH 1.2, 5.4, 7.2, and 8.5), demonstrating pH-dependent release behavior, with the highest release rate observed at acidic pH (pH 1.2). Error bars represent standard deviations from triplicate experiments.

interactions, with stirring and sonication enhancing drug adsorption by increasing surface area and drug molecules interaction [116,117]. On the other hand, IBU release from the $MAGSiAG_1$ nanocarriers is driven by diffusion and is pH-sensitive; at the acidic pH, the carboxyl group of IBUs is protonated, increasing its solubility and reducing its interaction with the carrier, leading to faster release. In neutral and mildly acidic pH, the carboxyl group is deprotonated, making IBU less soluble. Electrostatic and hydrophobic interactions with the dendrimer slow the release process [118]. At basic pH, IBU solubility is dramatically reduced due to nanocarrier interactions. The rapid release in acidic conditions suggests $MAGSiAG_1$ can effectively deliver IBU in gastric environments. Sustained release in neutral conditions demonstrates potential for drug delivery in systemic circulation [119]. In agreement with the general behavior of pH-responsive nanocarriers [120,121], the pH-dependent release profile of IBU from $MAGSiAG_1$ nanocarriers is highly relevant to the tumor microenvironment. Accelerated drug release is observed under acidic conditions (pH 5.0–6.5), which closely correspond to the extracellular pH typical of tumor tissues (6.2–6.8). In contrast, at physiological pH (~7.4), the release of IBU is significantly slower, ensuring minimal drug leakage in systemic circulation that minimizes side effects. Therefore, the pH-responsive release mechanism astonishing leverages the physiological conditions of the tumor microenvironment, effectively envisaging *in vivo* experiments where these nanocarriers would provide site-specific, controlled IBU delivery and then enhance therapeutic efficacy, while reducing off-target toxicity.

3.3. Cytotoxicity and cell viability studies on MCF-7 and EA.hy926 cellular lines

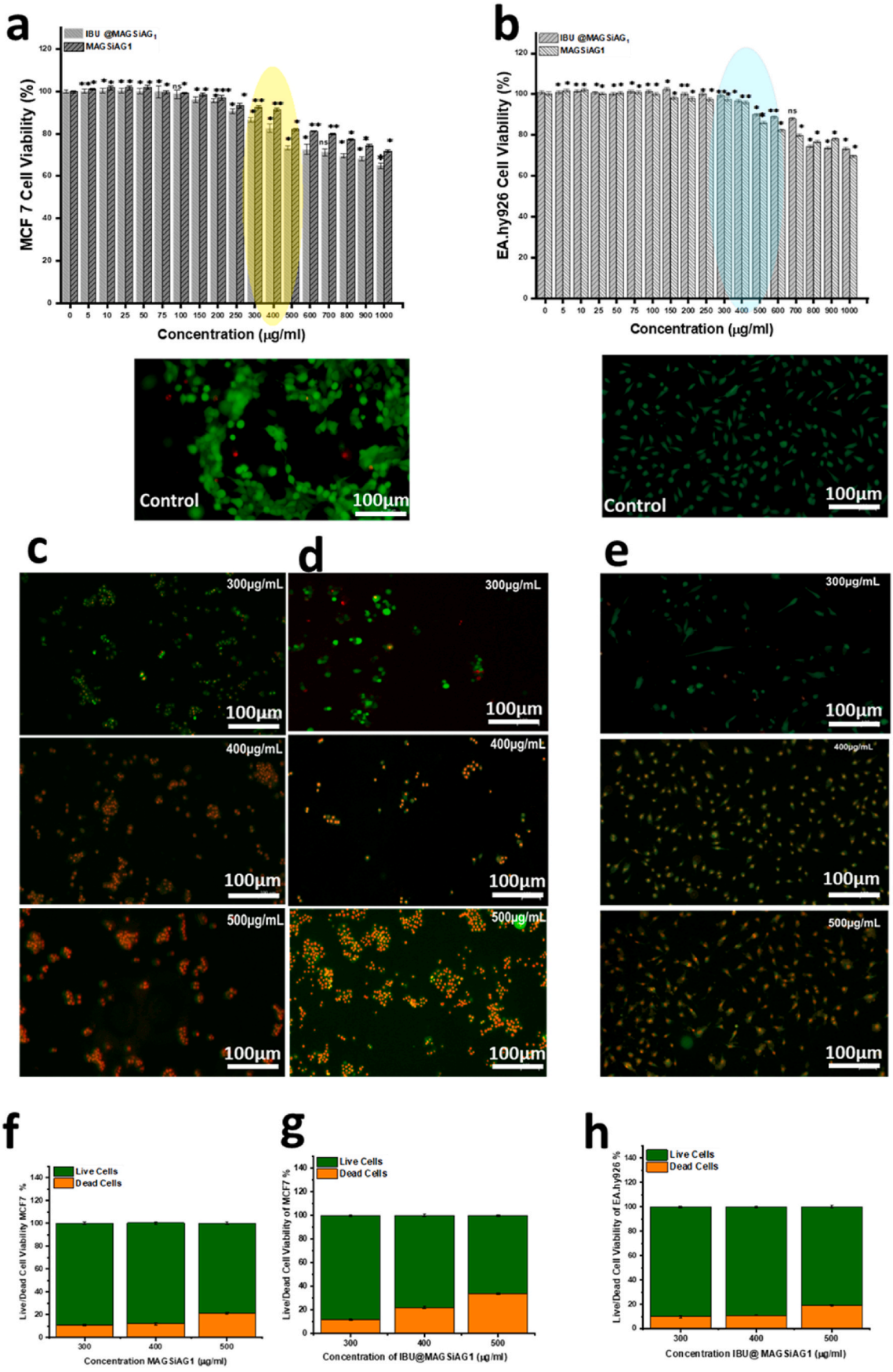
Fig. 5a show the cell viability (%) of MCF-7 breast cancer cells treated for 24 h with $MAGSiAG_1$ and $IBU@MAGSiAG_1$ at concentrations ranging from 0 to 1000 μg/mL, evaluated using the MTT assay. At low concentrations (0–100 μg/mL), $MAGSiAG_1$ nanocarriers maintain nearly 100% viability, showing excellent biocompatibility. $IBU@MAGSiAG_1$ nanocarriers are also close to 100% viability [87,122]. At moderate concentrations (150–300 μg/mL), $MAGSiAG_1$ maintain high cell viability (~98%), confirming its biocompatibility. The cell viability of $IBU@MAGSiAG_1$ nanocarriers slightly decrease (~95%), indicating moderate cytotoxic effects most likely due to IBU release. However, $IBU@MAGSiAG_1$ begins to show its cytotoxic potential at (300–500 μg/mL) concentrations, but side effects are still mild and at the same concentration $MAGSiAG_1$ remains less toxic (~85–95%). At the concentrations of (500–1000 μg/mL), $MAGSiAG_1$ still shows moderate cell viability (~75–90%), but $IBU@MAGSiAG_1$ exhibits significant cytotoxicity, with cell viability dropping to 60–80% due to the enhanced drug release. Therefore, at high concentrations, $IBU@MAGSiAG_1$ is more toxic than $MAGSiAG_1$ for inhibiting cancer cell growth due to extended release of the medicine. The presence of IBU enhances the cytotoxic effects of $MAGSiAG_1$, especially at concentrations above 300–400 μg/mL, where a significant reduction in cell viability is observed. However, at moderate concentrations (~90% cell viability), the cells remain metabolically active, which is ideal for applications such as imaging and hyperthermia, where both cellular uptake and viability are important. IBU cytotoxic effects are evident but not excessive, making $IBU@MAGSiAG_1$ nanocarriers effective against cancer cells, while maintaining a balance for theranostics. Higher concentrations (>400 μg/mL) might reduce cell viability too much, affecting imaging accuracy and therapeutic outcomes. Given so, for MCF-7 breast cancer cells, 200–400 μg/mL is envisaged as the concentration range for MRI and hyperthermia experiments. Overall, $MAGSiAG_1$ can be employed for biocompatible imaging purposes, while $IBU@MAGSiAG_1$ is suitable for therapeutic applications, where mild to moderate cytotoxicity is desired, due to its IBU release. This concentration range provides a balance between maintaining sufficient cell viability for experimental integrity and leveraging IBU therapeutic effects for cancer cell inhibition. The acidic environment of endosomes or lysosomes (pH ~5.5) triggers the IBU release from the dendrimer shell due to its pH-responsive structure [123,124].

In the evaluation of nanocarrier cytotoxicity and therapeutic potential, a comprehensive understanding of cell viability and morphological alterations is required. Therefore, the live/dead cell assay is performed on MCF-7 cells treated with $MAGSiAG_1$ and $IBU@MAGSiAG_1$ dendrimer nanocarriers at varying clinically-relevant concentrations (300, 400, and 500 μg/mL) to assess their effects on cell survival and morphology as showed in Figs. 5c and d. Fluorescence microscopy images reveal distinct patterns of viability, with $MAGSiAG_1$ showing predominantly green fluorescence at lower concentrations, thus indicating high live cells, while $IBU@MAGSiAG_1$ exhibits a dose-dependent increase in red fluorescence, thus suggesting enhanced cytotoxicity due to IBU release. At 300 μg/mL, cells treated with $MAGSiAG_1$ remain mostly viable with minimal red-stained dead cells, whereas $IBU@MAGSiAG_1$ reports a higher proportion of dead cells. At 400 μg/mL, an increase in red fluorescence is observed in both groups, with $IBU@MAGSiAG_1$ demonstrating a more pronounced cytotoxic effect. At 500 μg/mL, extensive red fluorescence is present in $IBU@MAGSiAG_1$-treated cells, indicating significant apoptotic or necrotic cell death, while $MAGSiAG_1$-treated cells retain a notable amount of green fluorescence. For $MAGSiAG_1$, the percentage of live cells remained ~ 95%, 88% and 85%, respectively. In contrast, $IBU@MAGSiAG_1$ treatment results in a decrease in cell viability, with 90%, 80% and 75%, demonstrating a higher cytotoxic effect due to drug release. These findings are consistent with the MTT assay results, thus validating the cytotoxicity of $IBU@MAGSiAG_1$ in a dose-dependent manner.

The MTT assay is performed on EA.hy926 endothelial cells to assess the cytotoxicity of $IBU@MAGSiAG_1$ nanocarriers. Since these vascular cells are among the first to encounter the nanocarriers during circulation to the tumor site, it is crucial to ensure that the carriers exhibit minimal off-target toxicity to healthy, non-cancerous cells. Therefore, Fig. 5b displays the viability of EA.hy926 cells treated with increasing concentrations (0–1000 μg/mL) of both $MAGSiAG_1$ and $IBU@MAGSiAG_1$ nanoparticles. Up to 300 μg/mL, cell viability remains above 98%, indicating excellent biocompatibility then a noticeable decline is observed beyond 500–600 μg/mL, with significant cytotoxicity ($^*p < 0.05$) at higher concentrations. It can be noticed that IBU loading does not dramatically alter biocompatibility at lower doses, but increases the cytotoxicity at higher concentrations. Live/dead staining images show green fluorescence for live cells and red/orange fluorescence for dead cells at 400 μg/mL as detailed in Fig. 5e. The untreated cells exhibit nearly 100% green fluorescence, confirming normal cell viability. As the concentration increases the proportion of red-stained (dead) cells rises, aligning both with the MTT data indicating reduced viability and also with the outcomes from MCF-7 cells. At higher concentrations, a significant number of cells exhibit compromised membrane integrity, confirming dose-dependent cytotoxicity. Biocompatibility of the nanocarriers with EA.hy926 cells at low concentrations and dose-dependent cytotoxicity at higher dosages are confirmed via the same test. The related histograms for the live and dead cells assay using imageJ software are shown in Figs. 5f,g,h. Table 1 that gathers the recent results in the field clearly underscores the IBU dose-dependent cytotoxicity and long-term chemo preventive effects, thus making it effective against breast cancer.

3.4. Relaxivity test and implications as MRI contrast agent

The chosen concentration range for MRI applications (150–400 μg/mL converted to mM) was selected based on a balance among biocompatibility, imaging efficacy, and therapeutic potential demonstrated by both $MAGSiAG_1$ and $IBU@MAGSiAG_1$ nanocarriers. Fig. 6a shows a linear relationship between relaxation rate 1/T2 (s^{-1}) and nanocarriers concentration for both $MAGSiAG_1$ and $IBU@MAGSiAG_1$, thus confirming their suitability as T2 MRI contrast agents. Considering the achieved values of the curve slope ($358.88 \pm 5\ mM^{-1}\ s^{-1}$ for $MAGSiAG_1$ and



(caption on next page)

Fig. 5. Cytotoxicity evaluation of $MAGSiAG_1$ and $IBU@MAGSiAG_1$ on MCF-7 cells and EA.hy926 cells at different concentrations (0–1000 μg/mL) after 24 h of incubation at 37 °C, 5% CO_2. **(a)** Cell viability of MCF-7 cells treated with $MAGSiAG_1$ and $IBU@MAGSiAG_1$ nanocarriers with the percentage of viable cells after 24 h of treatment. **(b)** Viability of EA.hy926 cells treated with $MAGSiAG_1$ and $IBU@MAGSiAG_1$. **(c,d)** Live/dead fluorescence microscopy images of MCF-7 cells treated with $MAGSiAG_1$ and $IBU@MAGSiAG_1$ at concentrations of 300, 400, and 500 μg/mL, and **(f,g)** related histograms. Scale bar: 100 μm. **(e)** Live/dead fluorescence microscopy images of EA.hy926 cells after treatment with increasing concentrations of $IBU@MAGSiAG_1$, and **(h)** related histogram. Scale bar: 100 μm. ImageJ software is used for quantitative analysis of live/dead cell viability. Data are presented as mean ± standard deviation from at least three independent experiments. Statistical significance is determined relative to the control (untreated) group, with significance levels indicated as follows: *p ≤ 0.05, **p ≤ 0.01, ***p ≤ 0.001; ns denotes non-significant differences (p > 0.05).

Table 1
Summary of studies on IBU effects on breast cancer in terms of dosages, outcomes, and mechanisms of action.

Dosage	Outcomes	Mechanism	ref
Regular IBU doses	64% reduction in breast cancer risk.	COX-2 inhibition reduces prostaglandin synthesis.	[125]
Daily NSAID intake	39% reduction in breast cancer risk. Dose-dependent effects observed.	COX-2 inhibition suppresses inflammation and growth.	[54]
Long-term IBU use	30–60% reduction in cancer risk. COX-independent mechanisms highlighted.	Apoptosis regulation via NF-κB, β-catenin, and PPARγ.	[126]
Standard doses	IBU interacts with COX-2 genetic variants to reduce cancer risk.	Genetic factors and COX-2 inhibition synergize effects.	[127]
Standard doses	COX and LOX inhibitors combined for enhanced chemoprevention.	COX-2 and LOX inhibition reduce inflammation.	[128]
>200 mg/day, long-term	Significant breast cancer risk reduction after 12 months of usage.	Prostaglandin suppression through COX-2 inhibition.	[129]
Standard NSAID doses	COX-independent apoptosis and cell cycle regulation observed.	Targets apoptosis and suppresses proliferation.	[130]
Therapeutic doses	Inhibits HER2+ tumor growth, reduces angiogenesis and aromatase activity.	COX-2 inhibition and prostaglandin reduction.	[131]
>300 μg/mL	$MAGSiAG_1$ shows high biocompatibility; $IBU@MAGSiAG_1$ demonstrates dose-dependent cytotoxicity with strong effects at >300 μg/mL.	Sustained release of IBU inhibits COX-2, reduces proliferation, activates apoptosis, and halts cell cycle progression.	This study

335.00 ± 49.8 mM^{-1} s^{-1} for $IBU@MAGSiAG_1$), the slightly lower value for $IBU@MAGSiAG_1$ indicates a minor reduction in relaxivity upon IBU loading, most likely due to changes in the surface environment or reduced accessibility of water protons to the magnetic core. Both formulations exhibit high values of *Pearson* r (>0.96) and R^2 (~0.94) correlation coefficients, indicating strong linearity and reliability of the relaxivity measurements. Fig. 6b demonstrates an increase in signal darkness (T2-weighted contrast) with increasing concentration of nanoparticles for both $MAGSiAG_1$ and $IBU@MAGSiAG_1$. $MAGSiAG_1$ appears slightly darker at equivalent concentrations compared to $IBU@MAGSiAG_1$, thus confirming the higher r_2 relaxivity [132]. The color-enhanced images of Fig. 6c visually confirm the concentration-dependent contrast enhancement. $IBU@MAGSiAG_1$ shows slightly reduced contrast compared to $MAGSiAG_1$ at equivalent concentrations, thus supporting the quantitative outcomes from r_2. $MAGSiAG_1$ nanocarriers exhibit high relaxivity due to their magnetic core. However, from the therapeutic point of view, $IBU@MAGSiAG_1$ combines imaging and therapeutic functionalities and a high r_2 relaxivity enables clear MRI visualization, while sustained IBU release provides anti-inflammatory and anticancer effects, as demonstrated by MTT assay results [133]. The selected concentration range (150–400 μg/mL) balances biocompatibility and imaging efficacy for the developed magnetite-based dendrimer nanocarriers. Compared to previously reported magnetite-based nanocarriers, both $MAGSiAG_1$-based dendrimer nanocarriers exhibit high T2 relaxivity, achieving therapeutic temperatures (~45 °C), while maintaining biocompatibility with endothelial cells and enabling moderate cytotoxicity in cancer cells at the optimal therapeutic behavior. This synergy of the developed nanocarrier empowers therapeutic efficacy and safety compared to existing magnetite-based nanocarriers.

3.5. Hyperthermia-driven multifunctional studies

Previous tests of relaxivity, cytotoxicity and cell viability on MCF-7 and EA.hy926 cells have confirmed that the optimal concentration range of $IBU@MAGSiAG_1$ nanocarrier for hyperthermia applications lies

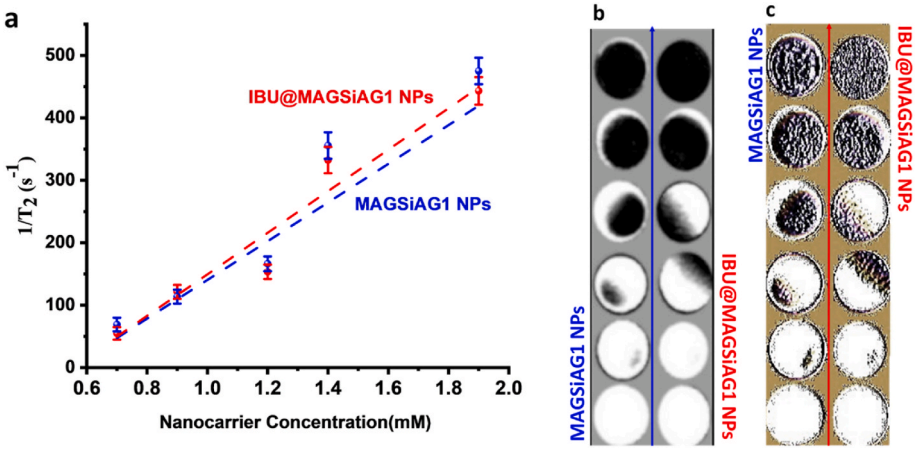


Fig. 6. (a) Relaxation rate ($1/T_2$) as a function of nanocarrier concentration (mM) for $MAGSiAG_1$ and $IBU@MAGSiAG_1$. Linear fits indicate the slope and intercept values with corresponding R^2 and *Pearson r* correlation values for both samples. T2-weighted MRI images of **(b)** $MAGSiAG_1$ and **(c)** $IBU@MAGSiAG_1$ at increasing concentrations.

in 250–400 μg/mL, which can also ensure effective cytotoxicity, strong MRI contrast and therapeutic efficiency. In fact, below 250 μg/mL, IBU release showcases insufficient therapeutic effect, while above 400 μg/mL, excessive cytotoxicity occurrs. At concentrations of 250–300 μg/mL, IBU@MAGSiAG$_1$ nanocarrier demonstrates mild to moderate cytotoxicity, reducing cell viability to approximately 85–95%, while maintaining excellent biocompatibility with MAGSiAG$_1$. This range provides a balanced approach for hyperthermia therapy, thus ensuring sufficient therapeutic effects without compromising experimental integrity. Strong T2-weighted MRI contrast is achieved at these concentrations, making this ideal for diagnostic imaging and treatment monitoring. For more aggressive hyperthermia treatments, a concentration of 400 μg/mL is selected, as IBU@MAGSiAG$_1$ exhibits significant cytotoxicity with reduced cell viability to 60–80%, while still providing excellent MRI contrast. This concentration is particularly effective in cases requiring intensive cancer cell inhibition due to the enhanced release of IBU. Under an AC magnetic field, the magnetic core of nanocarriers generates localized heat (41–45 °C) via *Néel* and *Brownian* relaxation, which enhances cell membrane permeability and weakens drug surface interactions, thereby accelerating pH-responsive release of IBU. Detailed explanation and developed protocols of assessment are provided in Supplementary Material (SM5).

Following above explanation, Fig. 7 displays the temperature changes as a function of time for MAGSiAG$_1$ and IBU@MAGSiAG$_1$ nanocarriers under varying magnetic field amplitudes (100 Oe, 125 Oe, and 150 Oe). The concentration of 400 μg/mL is selected as the optimal dosage for hyperthermia applications due to its ability to achieve a balance between effective cytotoxicity and excellent MRI contrast. At this concentration, IBU@MAGSiAG$_1$ nanocarrier exhibits significant heating efficiency under an AC magnetic field, thus reaching therapeutic temperatures of ~45 °C that are ideal for hyperthermia-based cancer treatment [134,135]. The choice of 400 μg/mL provides a powerful and multifunctional therapeutic approach that offers effective tumor ablation, while maintaining diagnostic accuracy and biocompatibility. Differently, MAGSiAG$_1$ nanocarrier demonstrates a slightly higher heating rate compared to IBU@MAGSiAG$_1$. Temperature increases to ~38 °C for MAGSiAG$_1$ and ~32 °C for IBU@MAGSiAG$_1$ after 500 s. At lower fields, the heating is less efficient due to reduced magnetic dipole

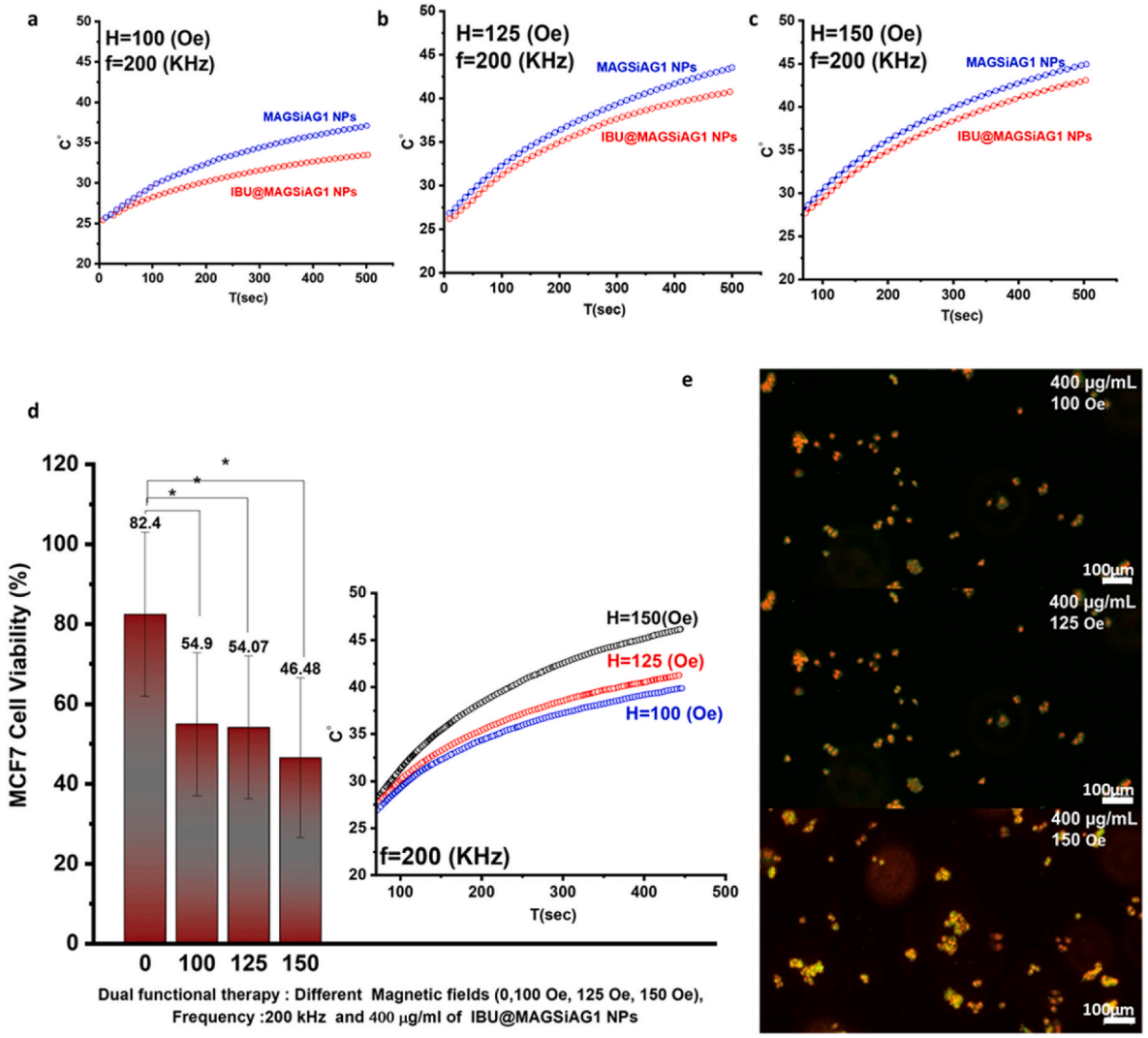


Fig. 7. Multifunctional therapy: Temperature increase (°C) as a function of time (T, sec) for MAGSiAG$_1$ and IBU@MAGSiAG$_1$ nanocarriers under different magnetic field intensities: **(a)** H = 100 Oe, **(b)** H = 125 Oe, and **(c)** H = 150 Oe, all at a frequency of f = 200 kHz. **(d)** Viability of cells as a function of increasing magnetic field intensity. Inset shows comparative heating profiles for unloaded and IBU-loaded MAGSiAG$_1$ nanocarriers at H = 150 Oe and f = 200 kHz. **(e)** Live/dead fluorescence images of treated MCF-7 cells with IBU-MAGSiAG$_1$, where green fluorescence represents viable cells, and red fluorescence indicates dead cells. The increase in red fluorescence intensity at 150 Oe suggests enhanced hyperthermia-induced cytotoxicity. Scale bar: 100 μm. Data are presented as mean ± standard deviation from at least three independent experiments. Statistical significance is determined relative to H = 0 Oe, with significance levels indicated as follows: *p ≤ 0.05 and ns denotes non-significant differences (p > 0.05).

alignment, and the impact of IBU in IBU@MAGSiAG$_1$ results in marginally lower heating efficiency. Both nanocarriers show improved heating compared to 100 Oe as it can be observed in Fig. 7a. MAGSiAG$_1$ reaches ~44 °C, while IBU@MAGSiAG$_1$ reaches ~40 °C after 500 s. The heating rate difference between the two samples narrows at this field strength, thus highlighting better performance of IBU@MAGSiAG$_1$ under intermediate field conditions as clearly shown in Fig. 7b. Fig. 7c details that, for the highest heating efficiency observed at 150 Oe, MAGSiAG$_1$ reaches ~45 °C, while IBU@MAGSiAG$_1$ reaches ~44 °C after 500 s. As the magnetic field increases from 100 Oe to 150 Oe, the temperature rise becomes more pronounced due to stronger magnetic dipole alignment and greater hysteresis losses. MAGSiAG$_1$ nanocarrier exhibits slightly higher heating efficiency across all field strengths due to higher saturation magnetization. This makes it more effective for general hyperthermia applications. On the other hand, IBU@MAGSiAG$_1$ nanocarrier showcases comparable heating performance with the additional therapeutic advantage of IBU release, thus making it suitable for targeted cancer therapy. The mechanism of hyperthermia can stem from *Néel* relaxation effect, since magnetic nanocarriers generate heat as their magnetic moments re-align with the AC magnetic field applied [136,137]. This mechanism is dominant for nanocarriers with smaller size and higher anisotropy energy. Conversely, the heat generation related to the *Brownian* relaxation occurs due to the physical rotation of nanocarriers in the liquid medium. This is influenced by particle size, shape, and surface modification (e.g., IBU loading). The present study remarkably confirms the potential of IBU@MAGSiAG$_1$ as a multifunctional agent for cancer hyperthermia and imaging. Fig. 7d demonstrates the cell viability of MCF-7 cells treated with the IBU@MAGSiAG$_1$ nanocarrier (400 μg/mL) under different magnetic field strengths (0, 100, 125, and 150 Oe) at a frequency of 200 kHz. Without any magnetic field (0 Oe), cell viability remains at 82.4%, thus highlighting the anticancer effect of the nanocarrier alone. However, under magnetic fields of 100 Oe and 125 Oe, cell viability significantly decreases to 54.9% and 54.07%, respectively, due to moderate cytotoxic effects caused by hyperthermia-induced cell damage and sustained drug release. At 150 Oe, cell viability drops further to 46.48%, which can stem from the enhanced heat generation and the synergistic effects of hyperthermia and IBU anti-inflammatory and pro-apoptotic properties. The temperature-time inset reported in Fig. 7d confirms that higher magnetic field strengths result in faster and higher temperature increases, with the 150 Oe field reaching therapeutic levels (~45 °C) more effectively. The magnetic nanocarriers rotate under an AC magnetic field, thus generating heat that denatures proteins, disrupts cell membranes, and triggers apoptosis, with controlled drug release which enhances the therapeutic effect. This remarkable multifunctionality ensures effective tumor ablation, demonstrating the potential of IBU@MAGSiAG$_1$ nanocarrier for hyperthermia-based cancer therapy. Fig. 7e displays fluorescence pictures of living and dead cells after the hyperthermia treatment. Elevated magnetic field strengths (100, 125, and 150 Oe) correspond to a gradual rise in red fluorescence that turns out to increasing cell mortality. The 150 Oe treatment group exhibits the most significant cytotoxicity, thus supporting the viability statistics presented before.

4. Conclusion

Hyperthermia-based therapy leveraging from magnetic nanomaterials is still facing critical clinical challenges, including achieving controlled and uniform heating within deep tumor regions, avoiding overheating of surrounding healthy tissues, maintaining nanoparticle stability and magnetic responsiveness under physiological conditions, and minimizing systemic toxicity and clearance issues. In this study, multifunctional dendrimer-functionalized nanocarriers that have been specifically engineered to overcome these limitations are developed and tested. The outcomes demonstrate, for the first time to the best of our knowledge, that these nanocarriers can be effectively employed for enhanced cancer treatment and imaging by integrating magnetic hyperthermia, pH-responsive drug delivery, and MRI diagnostics into a single therapeutic platform. The proposed nanocarrier showcases improved colloidal stability and biocompatibility, enabling uniform heat generation under an alternating magnetic field. The developed system can achieve therapeutic temperatures (~45 °C) without causing bulk overheating, indicating localized and controlled heating through *Néel* and *Brownian* relaxation mechanisms. Furthermore, the incorporation of IBU introduces synergistic anti-cancer and anti-inflammatory functions, while the pH-responsive release mechanism ensures selective drug delivery at the tumor site, minimizing systemic toxicity. In our experimental model, IBU@MAGSiAG$_1$ exhibits moderate cytotoxicity and excellent biocompatibility, yet reports substantial anti-cancer efficacy at 400 μg/mL, appropriate for intensive therapeutic treatments. Both nanocarriers display high relaxivity values (r_2), confirming their suitability as T2-weighted MRI contrast agents, with MAGSiAG$_1$ showing superior relaxivity due to its unmodified surface characteristics. It should be underlined that to strengthen the biological relevance of the outcomes achieved and also to assess the translational potential of the proposed multifunctional nanocarriers, additional cytotoxicity studies need to be conducted using other cancer cell lines and normal cells for comparative analysis. Overall, by integrating controlled hyperthermia with targeted drug release and real-time MRI monitoring, this system offers a novel and promising progress toward precision and personalized cancer therapy.

CRediT authorship contribution statement

Shadab Dabagh: Writing – original draft, Visualization, Methodology, Investigation, Formal analysis, Data curation, Conceptualization. **Hamed Ghorbanpoor:** Investigation, Formal analysis, Data curation. **Merve Nur Soykan:** Investigation, Formal analysis, Data curation. **Ayla Eker Sarıboyacı:** Visualization, Resources, Investigation, Formal analysis, Data curation. **Barbara Adinolfi:** Writing – review & editing, Methodology, Investigation. **Ambra Giannetti:** Writing – review & editing, Methodology, Investigation. **Zesen Li:** Visualization, Data curation. **Ni Lan:** Visualization, Data curation. **Bai-Ou Guan:** Writing – review & editing, Conceptualization. **Hüseyin Avci:** Writing – review & editing, Validation, Supervision, Methodology, Funding acquisition, Conceptualization. **Yang Ran:** Writing – review & editing, Supervision, Methodology, Funding acquisition, Conceptualization. **Francesco Chiavaioli:** Writing – review & editing, Validation, Supervision, Methodology, Funding acquisition, Conceptualization.

Ethical statement

Any animal or human involvement was planned in this study since all the experiments that support the findings were conducted *in vitro* or with the use of phantoms.

Declaration of generative AI and AI-assisted technologies in the writing process

During the preparation of this work the author(s) used Quill bot in order to improve the readability and language of the manuscript. After using this tool/service, the author(s) reviewed and edited the content as needed and take(s) full responsibility for the content of the published article.

Declaration of competing interest

The authors declare that they have no known competing financial interests or personal relationships that could have appeared to influence the work reported in this paper.

Acknowledgements

H.A. acknowledges the support received by The Scientific and Technological Research Council of Türkiye (TÜBİTAK), 1005-National New Ideas and Products, Grand ID: 123E013; TÜBİTAK, 3501-Career Development Program, Grand ID: 222M468; TÜBİTAK 1004 projects under the grant numbers of 20AG003 and 20AG031; Eskisehir Osmangazi University Scientific Research Projects Coordination Unit under grant number TOA-2022-2307 (BAP- the priority areas project (ONAP)). F.C. acknowledges the partial support received by the National Recovery and Resilience Plan (NRRP) through Mission 4, Component 2, Investment 1.1 under Grant 1409 in September 14, 2022, in part by the Italian Ministry of University and Research (MUR) through the European Union NextGenerationEU Project Title "Engineering Functional Metal Nanocluster-Protein Architectures for Bio(sensing and catalytic) applications" under Grant CUP B53D23013940006 and Grant 958 adopted on June 30, 2023.

Appendix A. Supplementary data

Supplementary data to this article can be found online at https://doi.org/10.1016/j.mtnano.2025.100726.

Appendix A. Supplementary data

The following is/are the supplementary data to this article.

Data availability

Data will be made available on request.

References

[1] J. Wei, et al., Magnetite nanoparticle assemblies and their biological applications: a review, Molecules 29 (17) (2024) 4160.
[2] K.E. Sapsford, et al., Functionalizing nanoparticles with biological molecules: developing chemistries that facilitate nanotechnology, Chemical reviews 113 (3) (2013) 1904–2074.
[3] A.K. Parashar, et al., Nanomaterials as diagnostic tools and drug carriers, in: Nanoparticles and Nanocarriers Based Pharmaceutical Preparations, Bentham Science Publishers, 2022, pp. 126–156.
[4] H.-S. Cho, et al., Fluorescent, superparamagnetic nanospheres for drug storage, targeting, and imaging: a multifunctional nanocarrier system for cancer diagnosis and treatment, ACS Nano 4 (9) (2010) 5398–5404.
[5] K.T. Nguyen, Y. Zhao, Engineered hybrid nanoparticles for on-demand diagnostics and therapeutics, Accounts Chem. Res. 48 (12) (2015) 3016–3025.
[6] L. Dong, et al., Copper carbonate nanoparticles as an effective biomineralized carrier to load macromolecular drugs for multimodal therapy, Chin. Chem. Lett. 34 (9) (2023) 108192.
[7] S. Natarajan, et al., Multifunctional magnetic iron oxide nanoparticles: diverse synthetic approaches, surface modifications, cytotoxicity towards biomedical and industrial applications, BMC Materials 1 (1) (2019) 1–22.
[8] K. Murase, et al., Control of the temperature rise in magnetic hyperthermia with use of an external static magnetic field, Phys. Med. 29 (6) (2013) 624–630.
[9] F. Oltolina, et al., Biomimetic magnetite nanoparticles as targeted drug nanocarriers and mediators of hyperthermia in an experimental cancer model, Cancers 12 (9) (2020) 2564.
[10] P.Q. Thong, et al., Multifunctional nanocarriers of Fe3O4@ PLA-PEG/curcumin for MRI, magnetic hyperthermia and drug delivery, Nanomedicine 17 (22) (2022) 1677–1693.
[11] R. Roohi, H. Emdad, K. Jafarpur, A comprehensive study and optimization of magnetic nanoparticle drug delivery to cancerous tissues via external magnetic field, J. Test. Eval. 47 (2) (2019) 681–703.
[12] W. Yu, et al., Advances in aggregatable nanoparticles for tumor-targeted drug delivery, Chin. Chem. Lett. 31 (6) (2020) 1366–1374.
[13] P. Abasian, et al., Polymeric nanocarriers in targeted drug delivery systems: a review, Polym. Adv. Technol. 31 (12) (2020) 2939–2954.
[14] X. Peng, et al., Engineered nanoparticles for precise targeted drug delivery and enhanced therapeutic efficacy in cancer immunotherapy, Acta Pharm. Sin. B (2024).
[15] M. Jeon, et al., Iron oxide nanoparticles as T1 contrast agents for magnetic resonance imaging: fundamentals, challenges, applications, and prospectives, Adv. Mater. 33 (23) (2021) 1906539.
[16] H.B. Na, I.C. Song, T. Hyeon, Inorganic nanoparticles for MRI contrast agents, Adv. Mater. 21 (21) (2009) 2133–2148.
[17] X. Men, et al., Activatable fluorescent probes for imaging and diagnosis of hepatocellular carcinoma, Journal of Innovative Optical Health Sciences 18 (3) (2025) 2530004, 2530004-25.
[18] X.-P. Li, et al., The emerging role of super-enhancers as therapeutic targets in the digestive system tumors, Int. J. Biol. Sci. 19 (4) (2023) 1036.
[19] J.B. Haun, et al., Magnetic nanoparticle biosensors, Wiley Interdiscip. Rev. Nanomed. Nanobiotechnol. 2 (3) (2010) 291–304.
[20] L. Koleva, et al., Erythrocytes as carriers: from drug delivery to biosensors, Pharmaceutics 12 (3) (2020) 276.
[21] S. Pandey, Advance Nanomaterials for Biosensors, MDPI, 2022, p. 219.
[22] S. Dabagh, et al., Functional nanomaterial coatings on optical fibers: toward enhanced biosensing performance, IEEE Sensors Reviews 2 (2025) 157–169.
[23] X. Li, et al., FUNMarker: fusion network-based method to identify prognostic and heterogeneous breast cancer biomarkers, IEEE ACM Trans. Comput. Biol. Bioinf 18 (6) (2020) 2483–2491.
[24] L. Zhou, et al., MAEL facilitates metabolic reprogramming and breast cancer progression by promoting the degradation of citrate synthase and fumarate hydratase via chaperone-mediated autophagy, FEBS J. 290 (14) (2023) 3614–3628.
[25] S. Caspani, et al., Magnetic nanomaterials as contrast agents for MRI, Materials 13 (11) (2020) 2586.
[26] B.A.A. Noor, Reduction Responsive Superparamagnetic Iron Oxide Nanoparticle Clusters for T2-T1 Magnetic Resonance Imaging, Concordia University, 2023.
[27] G.J. Soufi, et al., Nanoscale contrast agents for magnetic resonance imaging: a review, ACS Appl. Nano Mater. 5 (8) (2022) 10151–10166.
[28] P.B. Elming, et al., Hyperthermia: the optimal treatment to overcome radiation resistant hypoxia, Cancers 11 (1) (2019) 60.
[29] G. Nijhawan, S.S. Nijhawan, M. Sethi, Hyperthermia treatments, in: Noble Metal-Metal Oxide Hybrid Nanoparticles, Elsevier, 2019, pp. 241–263.
[30] G.P. Skandalakis, et al., Hyperthermia treatment advances for brain tumors, Int. J. Hyperther. 37 (2) (2020) 3–19.
[31] R. Bushra, et al., Recent advances in magnetic nanoparticles: key applications, environmental insights, and future strategies, Sustain. Mater. Technol. (2024) e00985.
[32] S.V. Spirou, et al., Recommendations for in vitro and in vivo testing of magnetic nanoparticle hyperthermia combined with radiation therapy, Nanomaterials 8 (5) (2018) 306.
[33] H. Gavilán, et al., Magnetic nanoparticles and clusters for magnetic hyperthermia: optimizing their heat performance and developing combinatorial therapies to tackle cancer, Chem. Soc. Rev. 50 (20) (2021) 11614–11667.
[34] Y. Yang, et al., Silica-based nanoparticles for biomedical applications: from nanocarriers to biomodulators, Accounts Chem. Res. 53 (8) (2020) 1545–1556.
[35] J. Park, et al., Cloaking silica nanoparticles with functional protein coatings for reduced complement activation and cellular uptake, ACS Nano (2020).
[36] Z. Gándara, N. Rubio, R. Castillo, Delivery of therapeutic biopolymers employing silica-Based nanosystems, Pharmaceutics 15 (2023).
[37] Y. Wang, et al., Charge-Reversal APTES-modified mesoporous silica nanoparticles with high drug loading and release controllability, ACS Appl. Mater. Interfaces 8 (27) (2016) 17166–17175.
[38] Y. Liu, et al., Kinetics of (3-aminopropyl)triethoxylsilane (APTES) silanization of superparamagnetic iron oxide nanoparticles, Langmuir : the ACS journal of surfaces and colloids 29 (49) (2013) 15275–15282.
[39] B. Sodipo, A. Aziz, One minute synthesis of amino-silane functionalized superparamagnetic iron oxide nanoparticles by sonochemical method, Ultrason. Sonochem. 40 (Pt A) (2018) 837–840.
[40] K. Abdollahi, F. Yazdani, R. Panahi, Fabrication of the robust and recyclable tyrosinase-harboring biocatalyst using ethylenediamine functionalized superparamagnetic nanoparticles: nanocarrier characterization and immobilized enzyme properties, JBIC, J. Biol. Inorg. Chem. 24 (2019) 943–959.
[41] A. Soozanipour, et al., Preparation of a stable and robust nanobiocatalyst by efficiently immobilizing of pectinase onto cyanuric chloride-functionalized chitosan grafted magnetic nanoparticles, J. Colloid Interface Sci. 536 (2019) 261–270.
[42] M. Pawlaczyk, G. Schroeder, Modification of magnetite nanoparticles with triazine-based dendrons and their application as drug-transporting systems, Int. J. Mol. Sci. 22 (2021).
[43] D. Nardo, et al., Cyanuric chloride as the basis for compositionally diverse lipids, RSC Adv. 11 (2021) 24752–24761.
[44] K. Abdollahi, F. Yazdani, R. Panahi, Covalent immobilization of tyrosinase onto cyanuric chloride crosslinked amine-functionalized superparamagnetic nanoparticles: synthesis and characterization of the recyclable nanobiocatalyst, Int. J. Biol. Macromol. 94 (Pt A) (2017) 396–405.
[45] S. Ray, et al., Dendrimer-and copolymer-based nanoparticles for magnetic resonance cancer theranostics, Theranostics 8 (22) (2018) 6322.
[46] E. Esmaeili, et al., Dendrimer functionalized magnetic nanoparticles as a promising platform for localized hyperthermia and magnetic resonance imaging diagnosis, J. Cell. Physiol. 234 (8) (2019) 12615–12624.
[47] A. Akbarzadeh, et al., Role of dendrimers in advanced drug delivery and biomedical applications: a review, Exp. Oncol. 40 (3) (2018) 178–183.
[48] K. Yamamoto, et al., New horizon of nanoparticle and cluster catalysis with dendrimers, Chemical reviews 120 (2) (2019) 1397–1437.
[49] K. Gerrans, et al., Silica nanoparticles functionalized with polyamidoamine (PAMAM) dendrimers as platforms for photoluminescence (PL) sensing of copper and cyanide ions, J. Colloid Interface Sci. 470 (2016) 276–283.

[50] R. Esfand, D. Tomalia, Poly(amidoamine) (PAMAM) dendrimers: from biomimicry to drug delivery and biomedical applications, Drug Discov. Today 6 (8) (2001) 427–436.
[51] B. Surekha, et al., PAMAM dendrimer as a talented multifunctional biomimetic nanocarrier for cancer diagnosis and therapy, Colloids Surf. B Biointerfaces 204 (2021) 111837.
[52] R.V. De Araújo, et al., New advances in general biomedical applications of PAMAM dendrimers, Molecules 23 (2018).
[53] C. Fokunang, et al., Overview of non-steroidal anti-inflammatory drugs (nsaids) in resource limited countries, Moj Toxicol 4 (1) (2018) 5–13.
[54] R.E. Harris, et al., Aspirin, ibuprofen, and other non-steroidal anti-inflammatory drugs in cancer prevention: a critical review of non-selective COX-2 blockade, Oncol. Rep. 13 (4) (2005) 559–583.
[55] R.E. Harris, Ibuprofen in the prevention and therapy of cancer, Ibuprofen: Discovery, Development and Therapeutics (2015) 518–546.
[56] C.A. Buciuman, et al., Exploring the cardiovascular safety profile of ibuprofen: insights from EudraVigilance database, Pharmaceuticals 18 (7) (2025) 1045.
[57] I. Umoh, et al., Histomorphological and biochemical alterations on the liver of wistar rats following Co-Administration of NSAIDs (Piroxicam, diclofenac and ibuprofen), Anatomy Journal of Africa 11 (2) (2022) 2175–2184.
[58] A. Agrawal, I. Fentiman, NSAIDs and breast cancer: a possible prevention and treatment strategy, Int. J. Clin. Pract. 62 (3) (2008) 444–449.
[59] Z. Zeng, et al., pH-Responsive nanoparticles based on ibuprofen prodrug as drug carriers for inhibition of primary tumor growth and metastasis, J. Mater. Chem. B 5 (33) (2017) 6860–6868.
[60] Z. Chai, et al., Doxorubicin delivered by redox-responsive Hyaluronic Acid-Ibuprofen prodrug micelles for treatment of metastatic breast cancer, Carbohydr. Polym. 245 (2020) 116527.
[61] Z. Li, et al., A nanomicellar prodrug carrier based on ibuprofen-conjugated polymer for Co-delivery of Doxorubicin, Front. Pharmacol. 9 (2018).
[62] E. Mauri, et al., Ester coupling of ibuprofen in hydrogel matrix: a facile one-step strategy for controlled anti-inflammatory drug release, Eur. J. Pharm. Biopharm. : official journal of Arbeitsgemeinschaft fur Pharmazeutische Verfahrenstechnik e. V (2019).
[63] A. Drinevskyi, et al., Activation of ibuprofen via ultrasonic complexation with silver in N-Doped oxidized graphene nanoparticles for microwave chemotherapy of cervix tumor tissues, ACS Biomater. Sci. Eng. 9 (1) (2022) 182–196.
[64] M. Talaei, S. Hassanzadeh-Tabrizi, A. Saffar-Teluri, Synthesis of mesoporous CuFe2O4@ SiO2 core-shell nanocomposite for simultaneous drug release and hyperthermia applications, Ceram. Int. 47 (21) (2021) 30287–30297.
[65] D. Zhang, et al., Magnetic nanocarriers for pH/GSH/NIR triple-responsive drug release and synergistic therapy in tumor cells, ACS Omega 9 (50) (2024) 49749–49758.
[66] B.M. Asghari, et al., Surface modification of nanodiamond with pH/thermo dual responsive polymer and hyper-branched dendrimer as a near-infrared photothermal-triggered drug delivery for cancer therapy, J. Mol. Liq. 390 (2023) 123155.
[67] H. Sun, et al., Cancer cell membrane-coated gold nanocages with hyperthermia-triggered drug release and homotypic target inhibit growth and metastasis of breast cancer, Adv. Funct. Mater. 27 (3) (2017) 1604300.
[68] S. Patra, et al., Dual-responsive polymer coated superparamagnetic nanoparticle for targeted drug delivery and hyperthermia treatment, ACS Appl. Mater. Interfaces 7 (17) (2015) 9235–9246.
[69] L. Crespo, et al., Peptide and amide bond-containing dendrimers, Chemical reviews 105 (5) (2005) 1663–1682.
[70] S. Fulda, K.M. Debatin, Apoptosis signaling in tumor therapy, Ann. N. Y. Acad. Sci. 1028 (1) (2004) 150–156.
[71] L. Garcia, et al., Fe3O4–SiO2 mesoporous core/shell nanoparticles for magnetic field-induced ibuprofen-controlled release, Langmuir 39 (1) (2022) 211–219.
[72] M. Ribeiro, et al., Xanthan-Fe3O4 nanoparticle composite hydrogels for non-invasive magnetic resonance imaging and magnetically assisted drug delivery, ACS Appl. Nano Mater. 4 (8) (2021) 7712–7729.
[73] S. Xuan, et al., Synthesis of biocompatible, mesoporous Fe3O4 nano/microspheres with large surface area for magnetic resonance imaging and therapeutic applications, ACS Appl. Mater. Interfaces 3 (2) (2011) 237–244.
[74] R.P. Pandey, et al., Experimental methods for the biological evaluation of nanoparticle-based drug delivery risks, Pharmaceutics 15 (2) (2023) 612.
[75] L. Slavov, et al., Raman spectroscopy investigation of magnetite nanoparticles in ferrofluids, J. Magn. Magn Mater. 322 (14) (2010) 1904–1911.
[76] L.K. Takanlou, et al., Heavy metal adsorption efficiency magnetic porous composites Fe3O4–SiO2–APTES, Desalination Water Treat. 184 (2020) 178–188.
[77] A. Karimian, et al., Fe3O4@ SiO2@ APTES@ MPIB-Mn (II) as an eco-friendly and magnetically recyclable nano catalyst for the green synthesis of various xanthene derivatives, J. Mol. Struct. 1297 (2024) 137014.
[78] M.R. Yazdani, et al., Fe3O4@ SiO2-APTES@ Isophthaloyl Dichloride/Montmorillonite magnetic nanoparticles for efficient removal of Pb2+ and Cd2+, Chem. Eng. Technol. 46 (9) (2023) 1896–1910.
[79] R. Ganjiselahchin, F. Soltanolkottabi, Removal of lead from aqueous solution by magnetic modified dendrimer (Fe3O4@ SiO2/(3-aminopropyl) triethoxysilane@ dendrimer/benzaldehyde), Chem. Eng. Commun. 211 (7) (2024) 1116–1127.
[80] R.B. Carvalho, S.V. Joshi, Ibuprofen isobutanolammonium salt: synthesis, thermal analysis, PXRD, FTIR and solubility investigations, J. Therm. Anal. Calorim. 139 (3) (2020) 1971–1976.
[81] K.M. Fahelelbom, et al., Utilization of green ATR-FTIR spectroscopic method for quantitative analysis of Ibuprofen tablets, Pharmacia 70 (2023) 999–1004.
[82] G. Oliveira-Filho, et al., Core-shell Au/Fe3O4 nanocomposite synthesized by thermal decomposition method: structural, optical, and magnetic properties, Appl. Surf. Sci. 563 (2021) 150290.
[83] S. Dabagh, et al., Silver-decorated and silica-capped magnetite nanoparticles with effective antibacterial activity and reusability, ACS Appl. Bio Mater. 6 (6) (2023) 2266–2276.
[84] S. Peiman, B. Maleki, Fe3O4@ SiO2@ NTMPThio-Cu: a sustainable and eco-friendly approach for the synthesis of heterocycle derivatives using a novel dendrimer template nanocatalyst, Sci. Rep. 14 (1) (2024) 17401.
[85] N. Karakurt, S. Erden, Poly (amidoamine) functionalized graphene oxide incorporated Carbon/Epoxy prepreg composites for enhanced electrical and thermal properties, Fibers Polym. 23 (13) (2022) 3569–3580.
[86] A.M. Abbas, et al., A novel ibuprofen derivative and its complexes: physicochemical characterization, DFT modeling, docking, in vitro anti-inflammatory studies, and DNA interaction, Molecules 27 (21) (2022) 7540.
[87] S. Dabagh, S.A. Haris, Y.N. Ertas, Engineered polyethylene glycol-coated zinc ferrite nanoparticles as a novel magnetic resonance imaging contrast agent, ACS Biomater. Sci. Eng. 9 (7) (2023) 4138–4148.
[88] S. Villa, et al., Functionalization of Fe3O4 NPs by silanization: use of amine (APTES) and thiol (MPTMS) silanes and their physical characterization, Materials 9 (10) (2016) 826.
[89] A.A. Chis, et al., Applications and limitations of dendrimers in biomedicine, Molecules 25 (17) (2020) 3982.
[90] P. Bonelli, et al., Ibuprofen delivered by poly (lactic-co-glycolic acid)(PLGA) nanoparticles to human gastric cancer cells exerts antiproliferative activity at very low concentrations, Int. J. Nanomed. (2012) 5683–5691.
[91] E.C. Dreaden, et al., Size matters: gold nanoparticles in targeted cancer drug delivery, Ther. Deliv. 3 (4) (2012) 457–478.
[92] Y. Cheng, et al., Pharmaceutical applications of dendrimers: promising nanocarriers for drug delivery, Front. Biosci. 13 (4) (2008) 1447–1471.
[93] M.P. Calatayud, et al., The effect of surface charge of functionalized Fe3O4 nanoparticles on protein adsorption and cell uptake, Biomaterials 35 (24) (2014) 6389–6399.
[94] G. Dzhardimalieva, et al., Colloidal stability of silica-modified magnetite nanoparticles: comparison of various dispersion techniques, Nanomaterials 11 (12) (2021) 3295.
[95] M.J. Khosravi, S.M. Hosseini, V. Vatanpour, Polyamidoamine dendrimers-Mil-125 (Ti) MOF embedded polyethersulfone membrane for enhanced removal of heavy metal, antibiotic and dye from water, J. Environ. Chem. Eng. 10 (6) (2022) 108644.
[96] J. Yang, et al., Surface-engineered dendrimers in gene delivery, Chemical reviews 115 (11) (2015) 5274–5300.
[97] S. Karimi, H. Namazi, Fe3O4@ PEG-coated dendrimer modified graphene oxide nanocomposite as a pH-sensitive drug carrier for targeted delivery of doxorubicin, J. Alloys Compd. 879 (2021) 160426.
[98] F. Hajizadeh, et al., Fe3O4@ SiO2@ PAMAM-G2 nanocomposite as sorbent for the extraction and preconcentration of estradiol valerate drug from human plasma samples, Microchem. J. 175 (2022) 107176.
[99] H.S. Far, et al., Magnetic metal–organic framework (Fe3O4@ MIL-101) functionalized with dendrimer: highly efficient and selective adsorption removal of organic dyes, J. Inorg. Organomet. Polym. Mater. 32 (10) (2022) 3848–3863.
[100] N. Fan, et al., The formation of a layer of Fe3O4 nanoplates between two carbon films, Carbon 45 (9) (2007) 1839–1846.
[101] L. Xu, et al., Formation, characterization, and magnetic properties of Fe3O4 nanowires encapsulated in carbon microtubes, J. Phys. Chem. B 108 (30) (2004) 10859–10862.
[102] A. Ángeles-Pascual, et al., Structure, magnetic and cytotoxic behaviour of solvothermally grown Fe3O4@ Au core-shell nanoparticles, Mater. Char. 142 (2018) 237–244.
[103] E.D. Pereira, et al., Study of controlled release of ibuprofen magnetic nanocomposites, J. Mol. Struct. 1232 (2021) 130067.
[104] F.O. Osorio, et al., Drug loading comparison of commercial ibuprofen on magnetite nanoparticles surface by UV–Vis spectrophotometry and acid-alkali titration by a factorial design of experiments, Open 14 (2023) 100193.
[105] A. Chakraborty, D.A. Islam, H. Acharya, Facile synthesis of CuO nanoparticles deposited zeolitic imidazolate frameworks (ZIF-8) for efficient photocatalytic dye degradation, J. Solid State Chem. 269 (2019) 566.
[106] L. Dian, et al., Cubic phase nanoparticles for sustained release of ibuprofen: formulation, characterization, and enhanced bioavailability study, Int. J. Nanomed. 8 (null) (2013) 845–854.
[107] S. Deng, et al., Anticancer drug release System based on Hollow Silica nanocarriers triggered by tumor cellular microenvironments, ACS Omega 6 (1) (2020) 553–558.
[108] N. Deirram, et al., pH-Responsive polymer nanoparticles for drug delivery, Macromol. Rapid Commun. 40 (10) (2019).
[109] X. Jia, et al., Hollow mesoporous Silica@Metal–Organic framework and applications for ph-responsive drug delivery, ChemMedChem 13 (5) (2018) 400–405.
[110] C. Gao, et al., Designable coordination bonding in mesopores as a pH-Responsive release system, Chem. Mater. 22 (19) (2010) 5437–5444.
[111] Y. Chang, et al., Cell-regulated hollow sulfur nanospheres with porous shell: a dual-responsive carrier for sustained drug release, ACS Sustain. Chem. Eng. 10 (16) (2022) 5138–5147.
[112] A.M. Khan, et al., ≪p>Artificial neural network (ANN) approach to predict an optimized pH-Dependent mesalamine matrix Tablet</P&gt, Drug Des. Dev. Ther. 14 (2020) 2435–2448.

[113] H. Bai, et al., A pH-sensitive graphene oxide composite hydrogel, Chem. Commun. 46 (14) (2010) 2376.
[114] R. Rojas, et al., Modeling drug release from a layered double hydroxide–ibuprofen complex, Appl. Clay Sci. 62 (2012) 15–20.
[115] T. Tran, et al., Temperature and pH responsive microfibers for controllable and variable ibuprofen delivery, Adv. Mater. Sci. Eng. 2015 (1) (2015) 180187.
[116] J. Zheng, et al., Study on ibuprofen/montmorillonite intercalation composites as drug release system, Appl. Clay Sci. 36 (4) (2007) 297–301.
[117] H. Alinezhad, et al., Magnetic solid-phase extraction of non-steroidal anti-inflammatory drugs from environmental water samples using polyamidoamine dendrimer functionalized with magnetite nanoparticles as a sorbent, Talanta 183 (2018) 149–157.
[118] F. Aboshnaf, The Synthesis and Application of Dendritic Polymer for Photodynamic Therapy, University of Sheffield, 2018.
[119] A. Agostini, et al., Synthesis and characterization of pH-sensitive drinkable nanoparticles for oral delivery of ibuprofen, Nanotechnology 29 (22) (2018) 225604.
[120] Z. Chen, et al., Advancements in pH-responsive nanocarriers: enhancing drug delivery for tumor therapy, Expet Opin. Drug Deliv. 20 (11) (2023) 1623–1642.
[121] N.M. AlSawaftah, et al., pH-responsive nanocarriers in cancer therapy, Polymers 14 (5) (2022) 936.
[122] J.H. Almaki, et al., Synthesis, characterization and in vitro evaluation of exquisite targeting SPIONs–PEG–HER in HER2+ human breast cancer cells, Nanotechnology 27 (10) (2016) 105601.
[123] Y. Jia, et al., Hyaluronic acid-based nano drug delivery systems for breast cancer treatment: recent advances, Front. Bioeng. Biotechnol. 10 (2022) 990145.
[124] I. Predarska, G.N. Kaluđerović, E. Hey-Hawkins, Nanostructured mesoporous silica carriers for platinum-based conjugates with anti-inflammatory agents, Biomater. Adv. (2024) 213998.
[125] R.E. Harris, J. Beebe-Donk, G.A. Alshafie, Reduction in the risk of human breast cancer by selective cyclooxygenase-2 (COX-2) inhibitors, BMC Cancer 6 (2006) 1–5.
[126] P. Matos, P. Jordan, Beyond COX-inhibition:'side-effects' of ibuprofen on neoplastic development and progression, Curr. Pharm. Des. 21 (21) (2015) 2978–2982.
[127] T.M. Brasky, et al., Genetic variants in COX-2, non-steroidal anti-inflammatory drugs, and breast cancer risk: the Western New York Exposures and breast cancer (WEB) study, Breast Cancer Res. Treat. 126 (2011) 157–165.
[128] R.E. Harris, J. Beebe, J.A. Schwartzbaum, Chemoprevention of breast cancer by cyclooxygenase and lipoxygenase inhibitors, World Academy of Sciences Journal 2 (1) (2020) 14–18.
[129] V. Ashok, et al., Selective cyclooxygenase-2 (COX-2) inhibitors and breast cancer risk, Breast 20 (1) (2011) 66–70.
[130] R.E. Harris, J. Beebe, G.A. Alshafie, Reduction in cancer risk by selective and nonselective cyclooxygenase-2 (COX-2) inhibitors, J. Exp. Pharmacol. (2012) 91–96.
[131] B. Arun, P. Goss, The role of COX-2 inhibition in breast cancer treatment and prevention, in: Seminars in Oncology, Elsevier, 2004.
[132] P. Gillis, F. Moiny, R.A. Brooks, On T2-shortening by strongly magnetized spheres: a partial refocusing model, Magn. Reson. Med.: An Official Journal of the International Society for Magnetic Resonance in Medicine 47 (2) (2002) 257–263.
[133] Z. Wang, et al., Controlled synthesis of MnFe 2 O 4 nanoparticles and Gd complex-based nanocomposites as tunable and enhanced T 1/T 2-weighted MRI contrast agents, J. Mater. Chem. B 2 (29) (2014) 4748–4753.
[134] T.M. Zagar, et al., Hyperthermia combined with radiation therapy for superficial breast cancer and chest wall recurrence: a review of the randomised data, Int. J. Hyperther. 26 (7) (2010) 612–617.
[135] F.S. Lobato, G.B. Libotte, G.M. Platt, Optimization of hyperthermia process applied to cancer treatment using multi-objective optimization differential evolution, J. Therm. Biol. 111 (2023) 103400.
[136] C.L. Dennis, R. Ivkov, Physics of heat generation using magnetic nanoparticles for hyperthermia, Int. J. Hyperther. 29 (8) (2013) 715–729.
[137] A. Rajan, N.K. Sahu, Review on magnetic nanoparticle-mediated hyperthermia for cancer therapy, J. Nanoparticle Res. 22 (2020) 1–25.